KØBENHAVNS UNIVERSITET

Assessment of Crowding by Viral Spike Protein Neuraminidase as a Potential Driver for Membrane Budding

Master's Thesis in Nanoscience

Victoria Thusgaard Ruhoff

The Niels Bohr Institute, University of Copenhagen

November 1, 2021

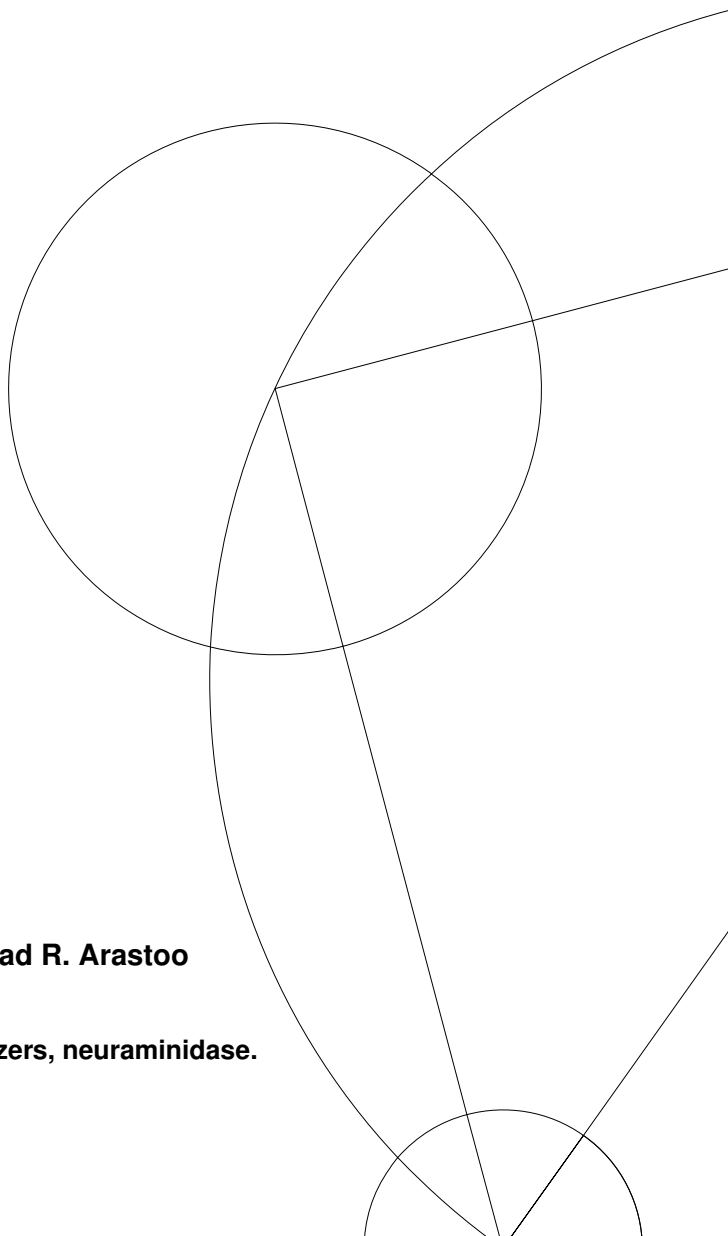

Supervisor: Pól Martin Bendix

Co-supervisors: Guillermo M. Pescador & Mohammad R. Arastoo

Key-words: Influenza A, budding, crowding, optical tweezers, neuraminidase.

Acknowledgements

I would like to extend my sincerest gratitude to my supervisor Pól M. Bendix Associate Professor at Niels Bohr Institute, University of Copenhagen, who despite sick leave has continued to inspire and advice me in the formulation of this project.

A special thanks to Postdoc Guillermo Pescador and Ph.D Mohammad Arastoo for the introduction to the numerous techniques used in the project. Their engagement in the thesis and immense guidance has helped me through the process in the best way possible. I also owe thanks to the Optical Tweezers group for allowing me access to the group labs and instruments to perform my experiments, and to the entire group for their advice and welcoming demeanour.

In addition, I would like to thank Helena Danielsen and Mads von Borries for their uplifting talks in the office, Younes Farhangibarooji and Natascha Leijnse for their technical advice and Ann-Katrine West for being the best possible lab cleaning partner. Besides, I thank Henrik Östbye and Robert Daniels at Stockholm University for providing the plasmid constructs that made this project possible.

Lastly I want to thank all my friends and family who supported me on this journey. It was a year riddled with ups and downs, and I would not have succeeded without the immense support I received. In addition, a thank you is directed at the Copenhagen Roundnet members, who have indulged me with energy and positivity throughout the project via great fun and physical exercise every week!

Abstract

Influenza A is a common viral infection spreading among humans and still remains a major societal challenge resulting in annual, global outbreaks with numerous casualties. A critical step in virus dissemination is the budding from the plasma membrane of infected cells. Despite extensive efforts, the mechanism underlying this viral budding event remains largely unsolved, however, the viral proteins NA, HA, M1 and M2 are known to be implicated in the facilitation of viral budding. In recent years, stochastic lateral pressure amongst membrane proteins, known as protein *crowding*, has evolved as a putative and effective driver of membrane bending and tubulation. The bulky ectodomains of the spike proteins NA and HA renders crowding a promising mechanism involved in the progression of viral budding. To gather evidence for this mechanism, optical tweezers were used to probe membrane bending in living cells expressing viral proteins. Specifically, membrane tethers were pulled from HEK cells transiently expressing NA, employing optical tweezers to allow for sensitive assessment of the membrane budding potential. Parallel imaging with confocal fluorescence microscopy allowed for correlation of the protein density with the force needed to extract membrane tethers. The results show a decrease in the tether equilibrium force as membrane coverage of NA increases, indicating an effect of crowding. Unexpectedly however, it was found that the average force (17.47 pN) measured for NA membrane tethers is significantly larger than for control cells (10.95 pN). This difference between transfected and wildtype cells is postulated to arise from a variability in membrane mechanics between the two groups, possibly due to side effects of the transfection protocol or due to an increase in the membrane bending rigidity (κ) upon expression of the NA transmembrane domain in the membrane. Conclusively, the presented assay is appropriate for the study of membrane crowding, and offers a novel method for quantitatively assessing the budding effect from viral envelope proteins.

Contents

Abbreviations

CLSM - Confocal laser scanning microscope

ESCRT - Endosomal sorting complexes required for transport

GFP - Green fluorescent protein

HA - Hemagglutinin

IDP - Intrinsically disordered protein

IQR - Interquartile range

IVA - Influenza virus A

NA - Neuraminidase

NP - Nucleoprotein

NEP - Nuclear export protein

OTs - Optical tweezers

PA - Polymerase acidic protein

PB1 - Polymerase basic protein 1

PB2 - Polymerase basic protein 2

QPD - Quadrant photodiode

SI - Supplementary information

TMD - Transmembrane domain

VP - Virus particle

VLP - Virus-like particle

vRNP - viral ribonucleoprotein particle

1 Introduction

Although human kind has experienced extreme technical advances in the last 50 years, we still lack a fundamental understanding of the immense complexity of biological systems. As we extend our understanding of the biochemical interactions between the cells of the human body, we have become extremely successful in the development of drugs and innovative treatments of everything from advanced cancer therapies to drug delivery systems and vaccine design. However, much is still to be uncovered. The recent COVID-19 pandemic has revealed how an organism as common and simple in structure as a virus, can leave the entire human race paralyzed in just a few months. In fact, there are more viruses on earth than stars in the universe[1], and although many of these are not pathogenic to humans, the globalisation of the world we live in has made it easy for viruses to rapidly evolve into a world wide pandemic, posing a great threat to human health.

Influenza virus A is one of the most common worldwide infections, and has been studied since its isolation in 1933[2]. Still, it was recently estimated that seasonal influenza infections are associated with an average of 390.000 annual deaths worldwide[3]. Even though multiple studies have been conducted, much is yet uncertain about the viral life cycle and function of the viral proteins. While it is known that influenza A virus spreads by budding from the plasma membrane of the host cell, the mechanism behind this crucial event, as well as the proteins involved, is still highly debated[4–7]. Since the budding event could be a potential target for combating viral infections and preventing the spread of the disease, understanding the underlying drivers of this event is of great interest. Despite the extensive efforts invested in this research, a deeper physical insight into the mechanism of viral budding still remains to be elucidated.

It is common for enveloped viruses to utilize the endosomal sorting complexes required for transport (ESCRT) of the host cell to bud, however influenza A particle release is not associated with the ESCRT pathway[8,9]. Various mechanisms for budding have been suggested, highlighting the importance of different viral proteins' intrinsic function and structure as reviewed by Nayak et al.[4]. The common conception is, however, that the viral proteins NA, HA, M1 and M2 are implicated in the process. It has been postulated that progeny virus particles bud from nanoscale raft domains[10], although this raft domain association property of the viral proteins have been put into question recently[11–13]. A putative mechanism for budding initiation, as the viral protein assembly on the plasma membrane, is surface protein *crowding*. Surface crowding is a phenomena describing the lateral pressure arising from stochastic collisions of proteins concentrated in a small area. Crowding has been shown to provide the energy required to form spontaneous membrane curvature and tubulation[14], and has thus become a highly discussed mechanism for the generation of membrane curvature in various systems[15]. As the spike proteins NA and HA have large bulky ectodomains, it is possible that they participate in budding initiation by crowding on the apical membrane.

So far, the conclusion regarding the budding requirements are vague at best. NA and HA have been shown to be necessary for budding[5], however expression of NA exclusively is demonstrated to allow formation of virus-like particles[16] (VLPs). On the contrary, M1 expressed alone also form VLPs[6] and NA deficient virus has been shown to retain function[17]. Evidently, more studies are needed to uncover the underlying interplay between the proteins. A combination of multiple mechanism is likely at play in effective budding and release. Nevertheless, it is very plausible that crowding of NA and HA contributes to the effective budding of progeny viruses.

The aim of this project is to provide further inside into the underlying mechanism of influenza virus budding. This is a critical step in the virus life cycle, involving complex membrane dynamics, and understanding this can not only lead to the development of antiviral drugs but also provide fundamental insight into the behavior and physics of membrane-shaping proteins. In this thesis the crowding effect of viral proteins will be studied by employing optical tweezers to probe the membrane dynamics.

Optical tweezers is a technique employing the trapping effect of a focused laser and is often used to probe biological systems as it is ultrasensitive, measuring forces in the pN range. Using a trapped bead to establish surface contact, the cell's plasma membrane can be pulled, forming a membrane tube with a radius and holding force which are determined by the mechanical properties of the membrane. The controlled generation of membranes tubes *in vitro* has been a useful assay in studying the dynamics of membrane associated proteins and their influence on membrane properties[18–20]. For instance, monitoring the equilibrium forces of membrane tethers has highlighted the curvature sensitivity of various proteins and scaffolding effects of curved proteins[12,21]. Recently, membrane tubes were utilized to demonstrate that viral protein NA is not curvature sensitive[12], however the effect of NA induced crowding on the plasma membrane remains to be assessed in a quantitative manner with ultrasensitive force sensor like optical tweezers.

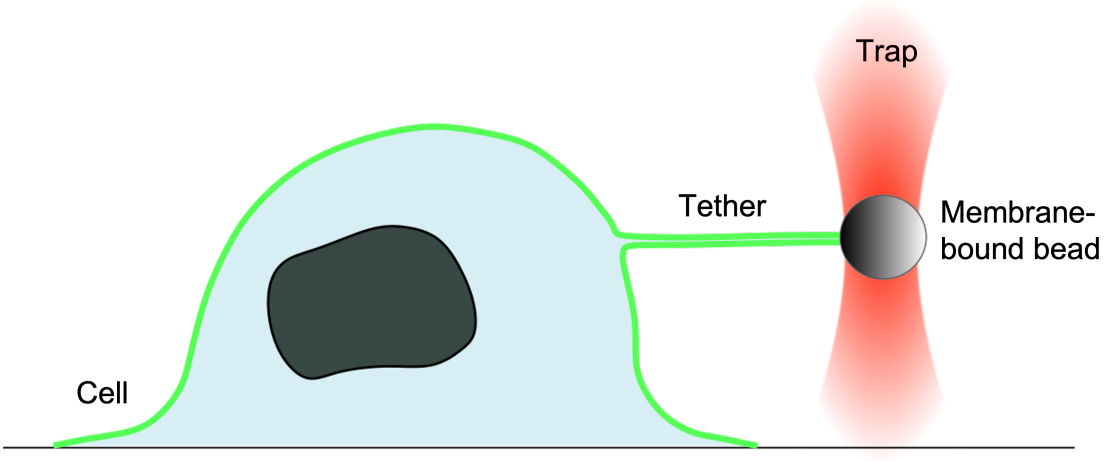

Figure 1: Schematic of tether pulled from a transfected cell on a glass surface. The green membrane indicates the expression of GFP-tagged NA.

In this thesis, the equilibrium force needed to hold a membrane tether is used as a means to measure the influence of NA expression on the membrane properties, with the goal of uncovering the extent of the crowding effect provided by the bulky spike protein. Tethers can be pulled from the plasma membrane of live cells expressing NA using an optical tweezer and a trapped membrane-binding bead (see figure 1). Simultaneous force probing will provide insight into the mechanics of the membrane budding effect. The thesis will focus on the isolated expression of NA in HEK cells and extract associated membrane deformation forces in the attempt of demonstrating the crowding effect of NA on the plasma membrane.

2 Biological background

2.1 Influenza A: stages of the viral life cycle

A virus is a simple organism incapable of surviving on its own and, like any organism, its goal is to replicate itself. Since a virus is merely a collection of genetic code protected by a shell, it is dependent on a host to live and spread. Viruses have therefore evolved to be extremely effective at hijacking the host cell's machinery for their own purpose. Thus the virion remains relatively simple in structure and often only encode very few genes.

One of the most common viral infections among humans is the influenza A virus. Influenza virus is responsible for numerous annual deaths around the globe and still poses a threat to humans. There are multiple types of influenza, namely A, B and C, where mainly A and B cause the yearly returning influenza outbreaks[22]. Already in 1933 was the first influenza virus A isolated from humans[2]. Since then has this parasitic organism been immensely studied, with the shared goal of understanding its mechanistic nature to prevent detrimental infections from spreading.

The virus consists of genetic material protected by a capsid and enveloped in a lipid membrane with spike proteins radiating outward on the entire surface[22] (see figure 2). Influenza virus is able to utilize the host cell machinery in an extremely effective manner. Because the virus contains negative-sense RNA, it needs to be transcribed in the host cell nucleus in order to assemble into new virus particles. As reviewed by Dou et al., this type of replication requires a network of complex cellular signaling for successful trafficking of viral components to occur[23]. Thus in reality, due to the intricacy of this viral life cycle, the majority of the released virus particles are either defective or non-infectious[4]. Generally the virus life cycle can be split into 3 overall steps: 1) Entry into host cell 2) Replication of genetic material 3) Release of progeny virus (see figure 2).

Entry into host cell: Adhesion, endocytosis and release or cargo.

In order to infect a host cell, the virus must first bind to the cell surface and be taken up by the cell. Influenza A virions are covered in spike proteins which are able to bind to surface receptors on the cell membrane. When the virus particle is attached, it enters the cell via the endocytic pathway, meaning it is engulfed and enters through an endosome. During endocytosis the endosome fuses with the lysosome, lowering the pH of the environment. This acidification triggers the uncoating and release of the viral RNA into the cytoplasm.

Replication of genetic material: Transcription, translation and transportation

After the genetic material is released into the cytoplasm, it is transported to the nucleus where the negative-sense RNA is transcribed to mRNA and duplicated for the progeny

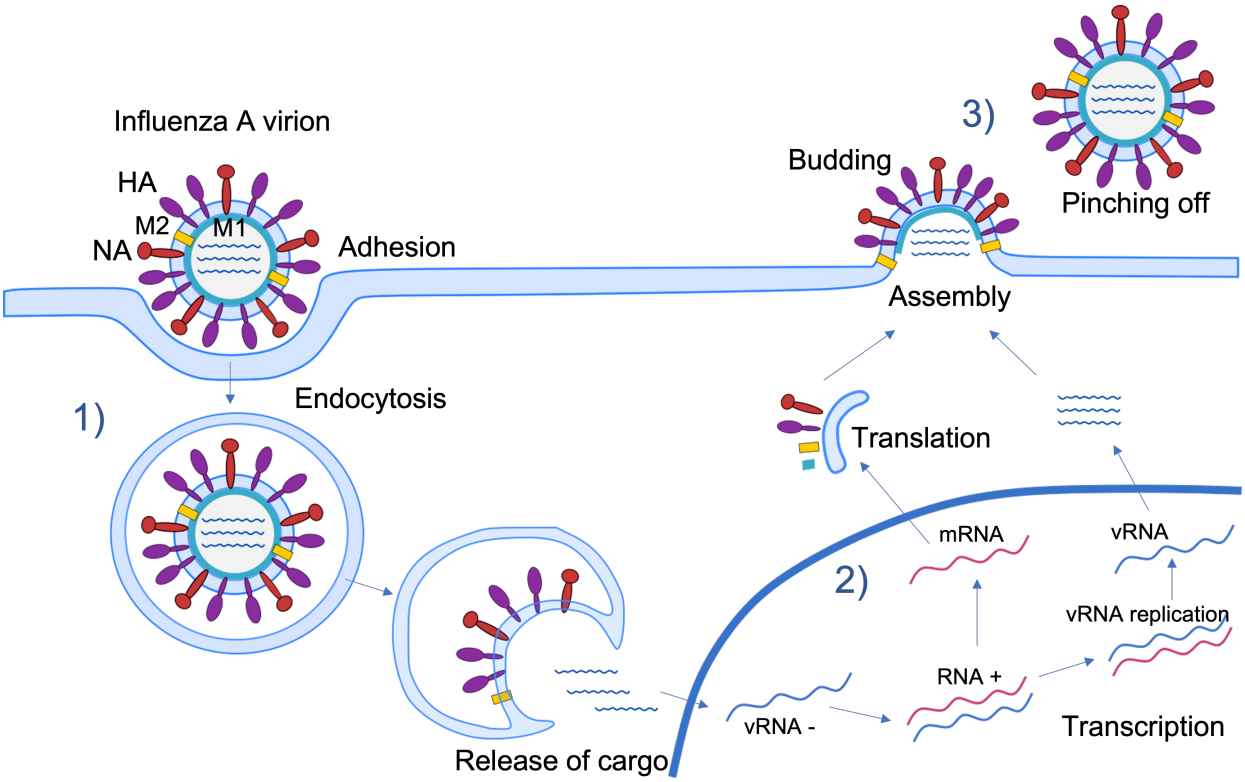

Figure 2: Schematic of the influenza A virus life cycle. The numbering 1-3 refers to the three overall events discussed in the text: 1) Entry into host cell. The particle first adheres via sialic acid residues and enters through endocytosis. Upon acidification in the lysosome the viral cargo is released into the cytosol. 2) Replication of genetic material. In the nucleus vRNA is replicated and transcribed to mRNA, where after translation occurs. 3) Release of progeny virus. The viral proteins assemble at the budding site, budding is initiated and eventually pinching off of the new progeny virus occurs. Figure adapted from Herold et al.[24], created with Inkscape[25].

virus[23]. The mRNA is then transported out of the nucleus where ribosomes translate the code and synthesize the viral proteins.

Release of progeny virus: Assembly, budding and pinching off

Once all the components of the virus particles have been constructed in the cell, assembly is needed to form a new virion. The envelope transmembrane proteins are recruited to the apical plasma membrane of the host cell, where they are believed to induce curvature in the membrane, initiating budding. The genetic material and capsid-enclosed proteins are translocated to the budding site to complete the virus particle. Various proteins are involved in the budding process which ends with the cleavage of sialic acid residues, allowing the progeny virus to pinch off from the host cell membrane and infect a new cell.

2.1.1 The budding event

Budding is an especially interesting part of the viral life cycle, as this step is key for the infection to spread. It is particularly interesting with a biophysics perspective, as it is this

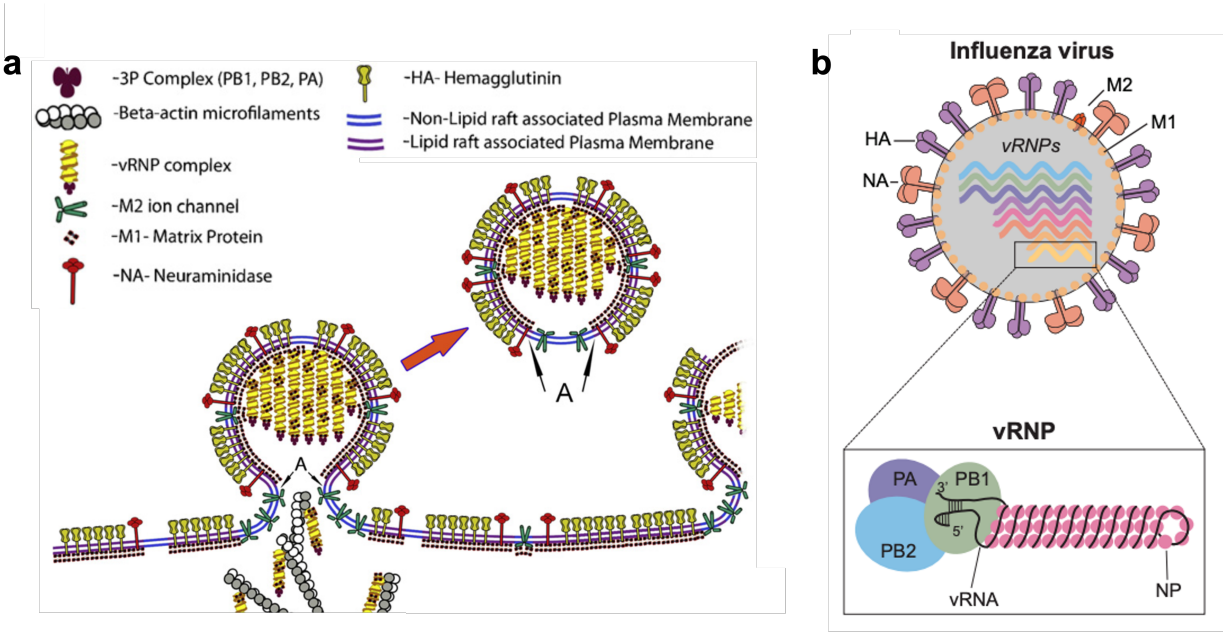

Figure 3: a) Illustration of protein assembly in viral budding, adapted from Nayak et al[4]. b) Simple schematic of the influenza viral particle, depicting the distribution of the viral proteins in the viral envelope and vRNPs. Reprinted from Dou et al[23].

step that involves the mechanics of the lipid membrane, which is a complex biodynamical platform riddled with physical interactions and forces between proteins and lipids. There are multiple ways to investigate the budding phenomena. The formation of virus-like particles by overexpression of specific viral components has provided an easy platform to investigate the role of the viral proteins but presents a technique devoid of cellular influence on genetic material. Thus reverse genetics have been extensively utilized to mutate and probe viral proteins, however both methods have limitations[4]. Common for much of the existing research on the budding phenomena, is the use of a generally acknowledged tool for studying the budding proteins. This tool is the morphological analysis of the progeny virus or buds at the membrane as a result of mutations.

Budding occurs when all the virus particle components are recruited to the budding site in the plasma membrane (see figure 3a). The budding event can be explained by three steps: 1) Association of viral proteins at the membrane 2) Formation of a budding vesicle containing the viral genome 3) Membrane scission and consequential release of the new virion from the cell. Extensive remodelling of the membrane is needed in order to overcome the membrane bending energy barrier and allow budding to occur. This step is critical and if we know how budding occurs it can help us create better antiviral agents, allowing us to fight pandemics in other ways than vaccines. Despite involvement of only 4 viral capsid associated proteins, the budding process remains enigmatic[4]. As an introduction to this interesting system, I will in the following describe the composition of the influenza virus and the function of the individual proteins.

2.2 Influenza A virion: structure & function of viral proteins

The influenza A virion is normally around 100nm in diameter and ranges in shape from spherical to pleomorphic. Influenza A is an enveloped virus, meaning the virion consists of a vesicle derived from the membrane of the host cell. The lipid bilayer contains essential viral proteins and encapsulated in the virion are 8 viral ribonucleoprotein particles (vRNP) that carry the genetic codes for the entire virus (11 genes) (see figure 3b). Each vRNP consists of a strand of viral RNA that is wrapped around the nucleoprotein NP and to some extent NEP, and packaged together in the center of the capsid. At one end of the vRNPs sits the RNA polymerase complex consisting of the last three viral proteins: PB1, PB2 and PA. The genetic material is encapsulated by a capsid structure of the membrane-associated matrix protein M1 just beneath the host-derived viral envelope. The envelope itself is believed to contain a mosaic of specific cholesterol-enriched lipid raft domains and non-raft domains[26,27], the ratio of which changes with temperature[4]. This envelope functions as an excellent, protective barrier for the virus[28]. Still the most striking feature of the influenza virion is the spike proteins covering the entire particle surface. These are the rodshaped HAs and the mushroom shaped NAs. They are thought to be anchored in lipid raft domains[29], though recent studies indicated that viral lipids might be predominantly in liquid disordered phase at physiological temperatures[28,30]. The spike proteins - a term that became infamous in the general public during the COVID-19 outbreak - are the parts of the virus that are recognized by the host immune system, eliciting an immune response to fight the infection. HA covers roughly 80% of the virion surface, and the ratio of HA to NA is around 5:1 but can vary. Besides NA and HA, the second matrix protein, M2, also assembles in the membrane, and all three are needed to form progeny viral particles[5]. While M1 does not sit in the membrane itself, both M1, M2, HA and NA have been shown to have an effect on the budding event[4,31]. Nevertheless, much is still unknown regarding their specific role in the mechanistic process. It is important to highlight that conflicting evidence exists regarding the specific function of the proteins. Rossman et al.[7] provides an excellent overview of the research conducted in regards to influenza virus budding, particularly highlighting the different results obtained for VLPs and virus-infection in cells. In viral like particles, single expression and/or co-expression of HA, NA and M2 have been demonstrated to be sufficient for VLP release[5], however in other studies M1 is also shown to induce budding and release independently of the other viral proteins[6]. Thus the environment in which the budding event is studied has a clear impact on the obtained results, and much is yet to be uncovered. Here I will present a brief overview of suggested behaviors of the involved proteins.

2.2.1 The spike proteins

The budding of progeny virions occur at the apical side of polarized cells. Therefor HA, NA, and M2 are transported to the apical plasma membrane[31]. It is believed that the

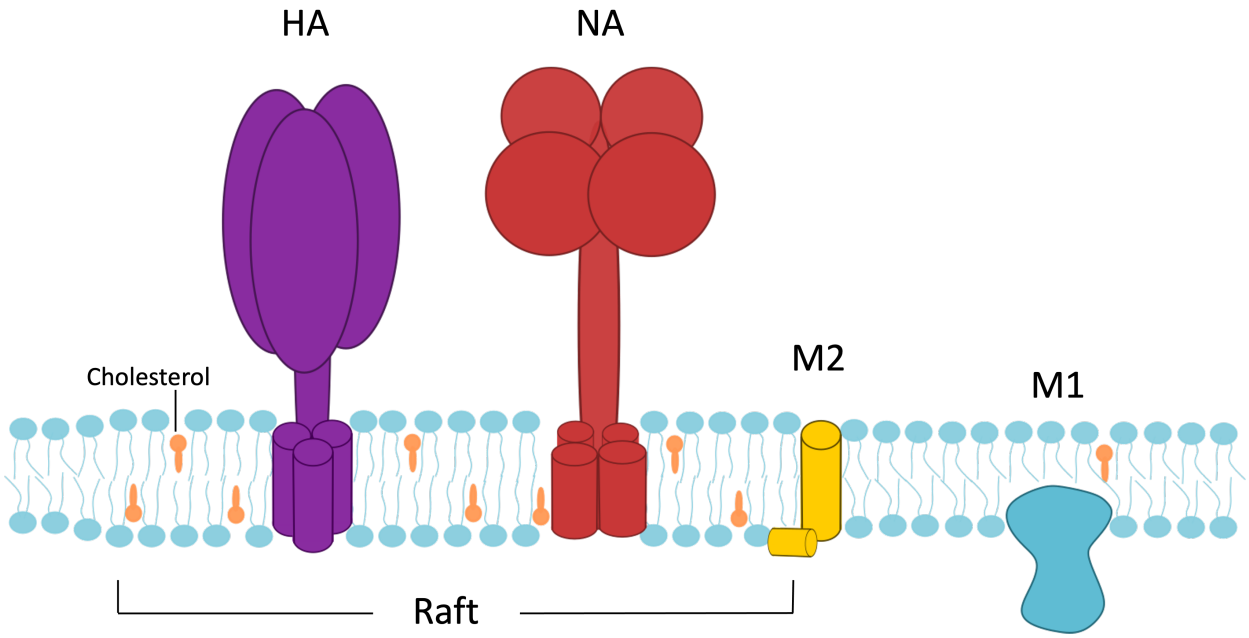

Figure 4: Schematic of the viral envelope associated viral proteins. HA and NA are here depicted in a raft domain, M2 at the edge of a raft and M1 associated with the inner leaflet of the membrane. HA is depicted as a trimer and NA as a tetramer. The membrane is simplified, only portraying cholesterol enrichment and saturated lipids to define the raft area. Figure is adapted from Veit et al.[10], created with Inkscape[25].

transmembrane domains of HA and NA associate with lipid rafts and that this interaction is responsible for the transport of the proteins to the apical side of polarized cells[32] (see figure 4).

Neuraminidase (NA) assembles as a tetramer in the plasma membrane[33]. The protein has a long stalk region and the tetramer has a large bulky ectodomain (figure 5a). NA covers roughly 20% of the virion surface area, and the distribution of NA and HA spike proteins across the membrane is not random. Instead NA proteins cluster together in smaller local domains, surrounded by HA proteins (see figure 3). An essential step that must transpire to allow newly made viral particles to dissociate from the plasma membrane is the cleavage of sialic acid residues from proteins and glycolipids. NA is an enzyme that is able to cut these sialic acids. Without this process it is not possible to have effective pinching off of the virion from the host plasma membrane and virus particles will tend to form aggregates[34]. Due to their large bulky ectodomains, the aggregation of NA together with HA in raft domains could also trigger initial membrane bending and consequently budding. Steric interaction of the tetramers (and trimers) could potentially give rise to a crowding effect with enough energy in the lateral pressure to overcome the membrane tension. This idea will be elaborated in section 2.4.

In this thesis, NA is the viral protein chosen for initial study of this crowding effect. To observe the localization of proteins and the protein density/expression in the membrane, the virus protein is tagged with GFP (see figure 5b). Thus the tetramer contains four GFP

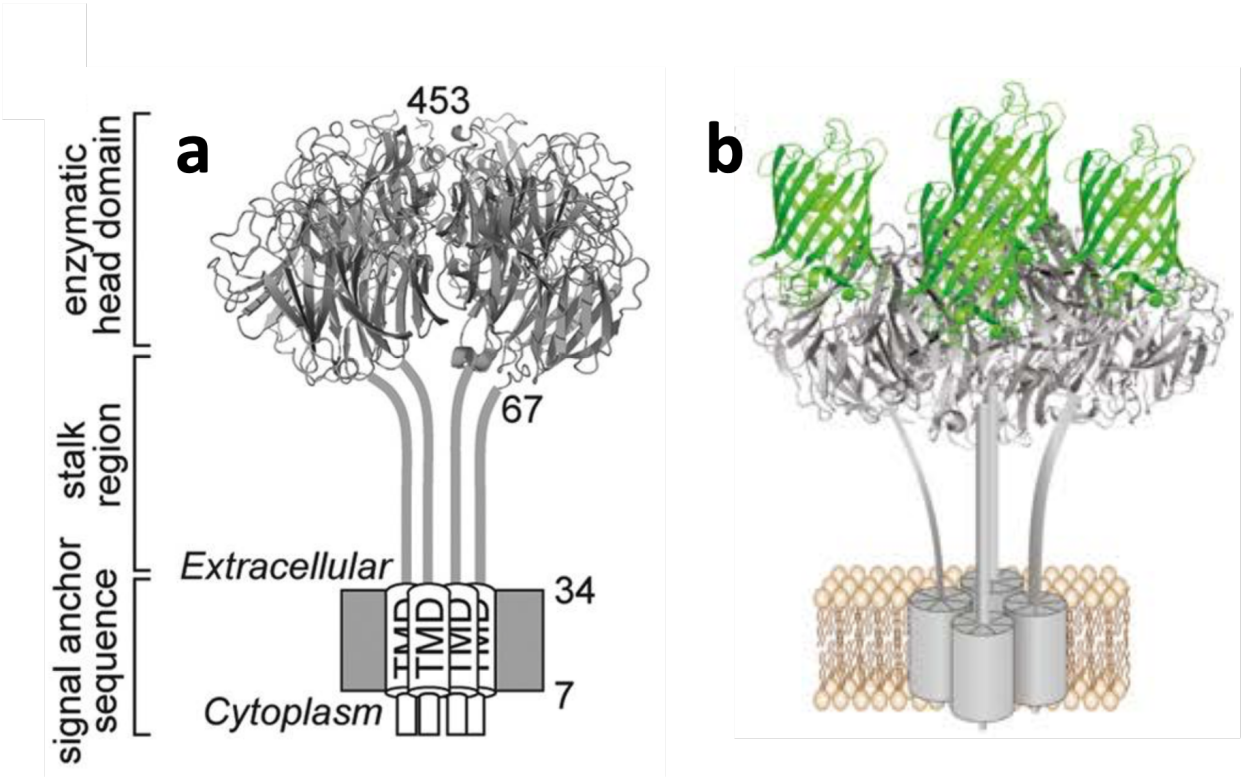

Figure 5: Structure of Neuraminidase. a) Structure with marked regions i.e. transmembrane domain, stalk region and enzymatic bulky head domain. Adapted from Nordholm et al[35]. b) Schematic of the GFP-tagged NA protein used in this thesis. Adapted from Guillermo[13].

proteins. This construct encoded in the plasmids used for transfection is provided by Henrik Östbye and Robert Daniels at Stockholm University.

Hemagglutinin (HA) is localized in the lipid membrane where it forms homotrimers with the characteristic spike feature. When HA binds to sialic acid receptors on the cell surface, receptor-mediated endocytosis is initiated. The virus particle thus enters into the host cell via an endosome. The low endosomal pH triggers a conformational change in HA, which allows the protein to mediate fusion of the endosomal and viral membrane. HA has been shown to be critical for virus budding[5], still only together with the four other proteins is viral infection shown to result in release of infectious progeny virus[7]. Like NA, the bulky ectodomain of HA could potentially lead to lateral pressure and be critical for membrane bending.

2.2.2 The matrix proteins

The two other proteins that are associated with the viral envelope are known as the matrix proteins (see figure 4). Neither of these contain large ectodomains, but provide other vital functions in the budding and release of virus.

Matrix protein 1 (M1) is a bi-function protein. In addition to binding to the vRNPs in the core, it also associated with the inner leaflet of the viral envelope and cytoplasmic tails of the viral transmembrane proteins mentioned above[4,36]. The peripheral protein has two

domains separated by a linker and forms a dimer[37]. M1 forms a bridge connecting the viral envelope with the core and upon oligomerization it supposedly clusters the viral proteins together. This clustering of M1 underneath the viral envelope membrane is also thought to induce membrane curvature and help initiate budding[38].

Matrix protein 2 (M2) is a proton-selective viroporin, meaning it functions as a tiny ion channel for H^+. Thus it can equilibrate pH across the viral membrane. The acidic environment in the endosome opens the M2 channel, allowing for protons to enter the virion core and this acidification results in the release of vRNP into the host cell cytoplasm. M2 is also postulated to play an important role in the final step of the budding event. M2 is shown to localize at the edge of the budding neck of forming virions[9] and composition analysis demonstrates that it is largely excluded from viral particles. Studies have shown that mutation or deletion of the tail of M2 leads to a change in virus morphology and release of only elongated virions, hence demonstrating the importance of M2 in the budding process.[39]. Thus M2 is believed to play a role in the membrane scission required to sever the budding virus neck and release the virion[9] (see figure 3a).

2.3 Lateral organisation of membranes

The plasma membrane is a lipid bilayer with hydrophilic surfaces and a hydrophobic inner section. It consists of various transmembrane proteins and lipids that are able to move freely in the lateral direction across the liquid disordered (Ld) phase of the plasma membrane. However, the different structures of membrane lipids allow for the emergence of transient and dynamic nanoscopic, relatively ordered, membrane domains known as membrane rafts and are used to compartmentalize cellular processes (see figure 6a). These domains are sterol- and sphingolipid-enriched and their existence is thought to be stabilized by lipid-lipid or lipid-protein interactions[10,42,43]. These rafts are liquid ordered (Lo) in nature and are a result of the organization of these Lo phases. They are restricted in mobility due to

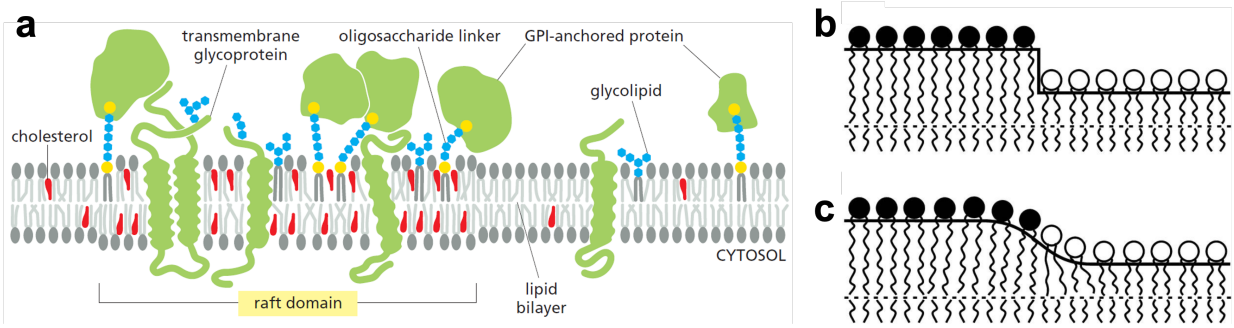

Figure 6: a) Classical illustration of a raft domain in the lipid bilayer, reprinted from Alberts et al.[40]. b) and c) Schematic of a lipid membrane demonstrating line tension which arises from height differences of domains. b) Sharp interface between an ordered and disordered phase. c) The hydrophobic mismatch between the lipids at the interface results in curving of the membrane raft phase to minimize the free energy. Reprinted from Kuzmin et al[41].

the dense packing of cholesterol and sphingolipids, and can move as a unit laterally in the Ld membrane. When these two membrane domains meet in model systems, a line tension is created due to the mismatch of height between the domains (the saturated fatty acid lipids are longer) (see figure 6b,c). The system attempts to reduce the hydrophobic-hydrophillic interaction by bending the raft domain. Many techniques have been developed to study raft domains including extraction by detergents and phase separation in giant unilamellar vesicles (GUVs)[42,44]. Characterizing the temporal and spatial compartmentalization of lipid rafts is still a vexing issue, however researchers agree that raft organization is an essential part of membrane trafficking and biological functions[42,45].

2.3.1 Raft domains as a budding platform

NA and HA have long been postulated to be recruited by lipid raft domains in the plasma membrane and have been shown to associated with lipid raft domains in *in vitro* studies[32,38,46]. It is suggested that the association of NA and HA in the raft domains functions to stabilize the domains, forming a 'long-lived' domain from which budding can occur. It is possible that the inherent curve from line tension in raft domains is stabilized and exaggerated by the raft association of these proteins. This viral protein-rich raft domain is referred to as a 'budzone'. However a study performed by Nikolaus et al.[47] and recently published studies by Arastoo- & Moreno-Pescador et al. show partitioning of the virus proteins HA and NA, respectively, into non-raft like domains in isolated plasma membranes which were fused to model membranes exhibiting large-scale phase separation.[11,12]. This enigmatic difference in the measured association of viral proteins with raft and non-raft domains can potentially be explained by different lipid packing organisation in the various membrane types or could originate from unexplored protein-protein effects which could facilitate translocation of NA and HA into Lo membrane phases, but is still a very debated topic[10].

In summary, when analysing virus particles the spike proteins have been shown to localize in membrane rafts (see figure 4). Therefore it is believed that the spike proteins initiate the budding event from the raft domains. This notion is supported by Takeda et al. who showed that non-raft associated HA mutants resulted in reduced budding of virus particles from infected cells[48]. Exactly how the budding occurs is still discussed, and in the following I will present a well-discussed mechanism for budding.

2.4 Crowding: A putative mechanism in membrane budding

It has long been thought that specific structural features are needed in order for proteins to facilitate breakage of the membrane bending energy barrier. Membrane bending and fission has therefore generally been attributed to three main functions: hydrophobic insertions (wedges), cylindrical scaffolds and cytoskeletal assemblies[14,49–51]. However during the last decade, a body of research has emerged introducing 'crowding' as a stochastic physical

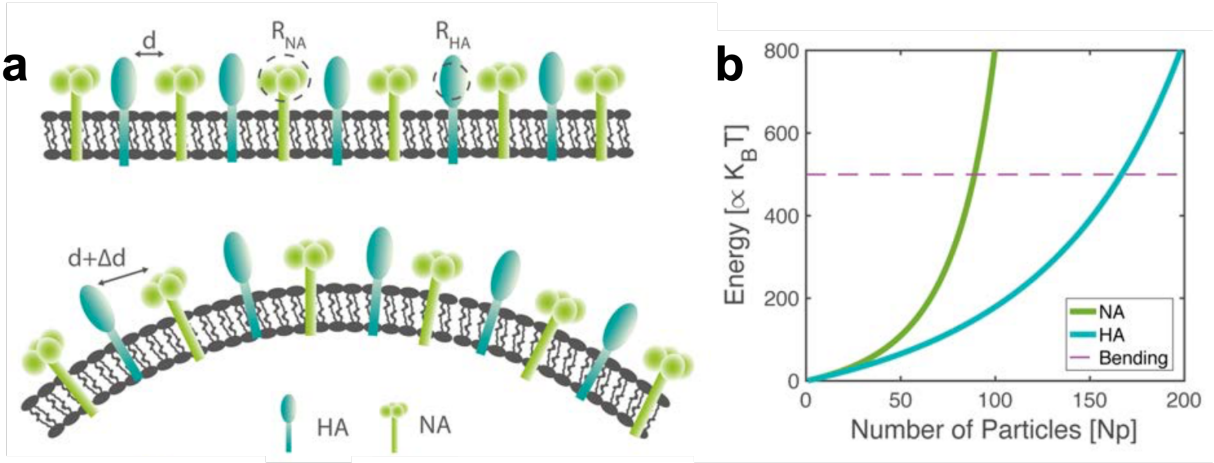

Figure 7: Membrane bending by crowding. a) Schematic of NA (green) and HA (blue) proteins laterally confined i.e.*crowding* on the membrane and inducing membrane bending. b) Plot of energy vs. particles (surface coverage). A larger number of HA proteins are needed to break the energy barrier compared to NA. This is due to the HA ectodomain being less bulky compared to NA. The dashed line (purple) represents the energy threshold typical for plasma membrane bending - ca. 500 k_BT. Plot was generated based on the Carnahan-Starling equation (parameters: $d_{vesicle} = 100$ nm, $R_{NA} = 9$ nm, $R_{HA} = 5$ nm. See Guillermo[13]) for details. a) and b) adapted from Guillermo[13].

mechanisms driving spontaneous membrane curvature and tubulation[14,52]. Proteins lacking the classical structural features associated with membrane bending have been shown to induce surface tubulation[53,54].

Surface crowding is a phenomena which describes the physical effect of concentrating proteins in a small area. Transmembrane proteins in the lipid bilayer are free to diffuse, resulting in continuous lateral protein-protein collision on the membrane surface. These collisions raise the steric pressure on the membrane and will increase non-linearly with increasing protein coverage[14]. When the pressure reaches a threshold, the membrane will bend to expand the area per protein on the membrane surface (see figure 7a). This crowding effect is independent of curvature sensing. Thus it can be attributed simply to the confinement and lateral steric forces of surface bound proteins[14,52,55]. We can think of this effect with a simple geometric reflection. Modelling the surface proteins as non-interacting spheres, the energy generated by crowding can be estimated using the Carnahan-Starling equation of state[56]. Doing so for the two viral spike proteins NA and HA, it was estimated that around 40% coverage was needed for membrane bending[13] (see figure 7b). Due to the different structures of NA and HA, it was determined that one NA protein was needed for every three HA (1:3), which mimics the 1:5 ratio observed on virus particles.

As crowding is an entirely stochastic processs, the cell must employ strategies to organize the protein collisions to the desired fission locations. This confinement could be introduced by membrane rafts in the plasma membrane, and *in vitro* research has shown that such domain confinement can drive spontaneous curvature formation[55]. Interestingly, the existence of phase separated domains such as those forming lipid rafts is opposed by protein and polymer crowding, as the steric pressure exceeds the enthalpy of membrane mixing[57].

This suggests that the ability of rafts to resist steric pressure and maintain phase separation from steric pressure depends on their composition[58]. In turn, this aids the hypothesis that the association of NA and HA with the lipid rafts stabilize them and drives the coalescence of these into larger, stronger domains able to confine the steric pressure to allow budding to occur. However, recent evidence showing that HA and NA are not associated with raft Lo domains at physiological temperatures in model systems calls this theory into question[11,47]. Some degree of domain organization is however extremely plausible, as the crowding effect is predicted to be significantly larger when proteins are confined to the budding area by a diffusion barrier[59]. M1, whose role is still debated, could have the effect of a diffusion barrier, as M1 has been proposed to oligomerize and cluster the viral proteins at the budding site[10,60]. Much is still to be investigated in order to establish how protein lateral confinement and crowding may play a role in virus budding. In this thesis, plasma membranes embedded with the viral protein NA are probed to uncover any spontaneous curvature formation from lateral crowding of this protein on the surface.

3 Experimental techniques

3.1 Fluorescence Microscopy

Fluorescence microscopy is a technique in which the properties of fluorophores are exploited to visualize objects that are invisible to the naked eye. Simply stated, in a fluorescence microscope a collection of mirrors and lenses are used to focus a light source of a certain wavelength onto a fluorescently labeled sample. Excitation of the fluorophores in the sample results in the re-emittance of light at a different wavelength, which using filters and mirrors can be directed to the detector. State-of-the-art fluorescent microscopes can be very advanced, and the precise specifications of lenses and mirrors can be extremely complex depending on the experimental needs and required resolution[61].

The existence of fluorescence microscopy techniques relies on the ability of a molecule, a fluorophore, to absorb energy at one wavelength and emit it again at a different wavelength. A fluorophore can only absorb a certain photon energy due to the inherent electronic transitions in the molecule. Jablonski diagrams can be used to visualize such transitions[63] (see figure 8). After a fluorophore is excited from its ground state S0 to its excited state S1, it undergoes internal conversion, where the electron relaxes to the lowest vibrational sub-level of the first excited level in the electronic state before experiencing radiative decay[61] (see figure 8). It is this specific radiative transition that is termed "fluorescence". The slight relaxation in the energy means that the light emitted is always of a shorter wavelength than the light absorbed, since energy and wavelength are inversely proportional according to Planck's law. The resulting difference in the absorbed and emitted wavelength is known at the Stokes Shift, and is characteristic for the type of fluorophore used and the conditions in the sample. In fluorescence microscopy, it is this essential property of fluorophores that allows us to separate the emitted light from the light source using filters and thus provide clear and bright fluorescence images with good contrast. In addition multiple fluorophores can be imaged simultaneously if they have distinct absorption and emission spectra, by using specialized filters called filter cubes. The emission of fluorescence is a fast process on the order of 10^{-12} to 10^{-6} s, and the efficiency of it is essential for imaging. The efficiency of a fluorescence process is indicated by the so-called quantum yield of the fluorophore. An ideal fluorophore will emit one photon for each absorbed, resulting in a quantum yield of 1. However this is rarely the case due to the loss of energy from the Stokes Shift. As all electrons must eventually decay by some process, the quantum yield can be described using the radiative k_r and non radiative decay

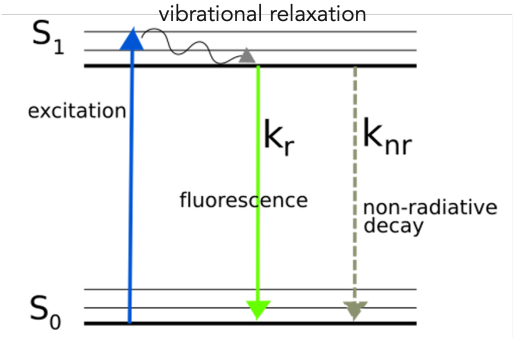

Figure 8: Illustrative Jablonski diagram showing the relation between rates used to express quantum yield. Reprinted from Ruhoff[62].

k_{nr} rate constants[64]

$$\Phi = \frac{k_r}{k_r + k_{nr}}$$

with the corresponding lifetime defined as

$$\tau = \frac{1}{k_r + k_{nr}}.$$

Both properties influence our ability to effectively detect the fluorophores in the sample.

Naturally, quantum yield and lifetime are essential properties to consider when choosing fluorophores, however, other factors such as size, toxicity and stability are important in experimental design as well. A common weakness of (many) fluorophores is the light-induced chemical damage that arises from long exposure to light, known as photobleaching[64]. Stable fluorophores are thus desirable for time-consuming experiments, unless photobleaching can be ingeniously exploited as is the case for Flourescence Recovery After Photobleaching (FRAP) experiments[65]. Photobleaching can also to some extent be controlled by the chemical environment in the experiment[66]. The best fluorophores are often inorganic and synthetically created, such as Quantum dots. These fluorophores are extremely stable, have excellent quantum yields, and can be tuned to a specific wavelength, giving researchers the ability to modify them for their experimental needs. However, these inorganic fluorophroes are often toxic to living organisms, and are therefore not ideal when conducting live imaging experiments[67]. Green fluorescent protein (GFP) is an alternative, naturally extracted fluorophore from jellyfish, which is widely used for live cell imaging across scientific research fields[68]. The downside of using a fluorescent protein such as GFP is that it is often comparable in size to the cellular objects under study e.g. proteins, substrates, drug delivery vehicles. The size of the fluorophore becomes important when studying molecular dynamics, as it can potentially slow down the subject. In addition, the impact of the large fluorophore on binding properties or protein function needs to be evaluated when designing the experiments.

3.2 Confocal laser-scanning microscopy

Simple microscopy techniques such as widefield fluorescence or brightfield microscopy are limited in resolution, as out-of-focus light is collected during sampling and disturbs the image contrast. In widefield fluoresence, the information gathered along the Z-axis of the sample, is collapsed into a 2D image. This 'merging in the Z-direction' lowers the image resolution by smudging the information. To obtain a higher contrast image, a very thin slice of information in the X-Y plane can be extracted, by eliminating the obscuring light above and below the focus plane of the sample from the image detection[61]. This is exactly the

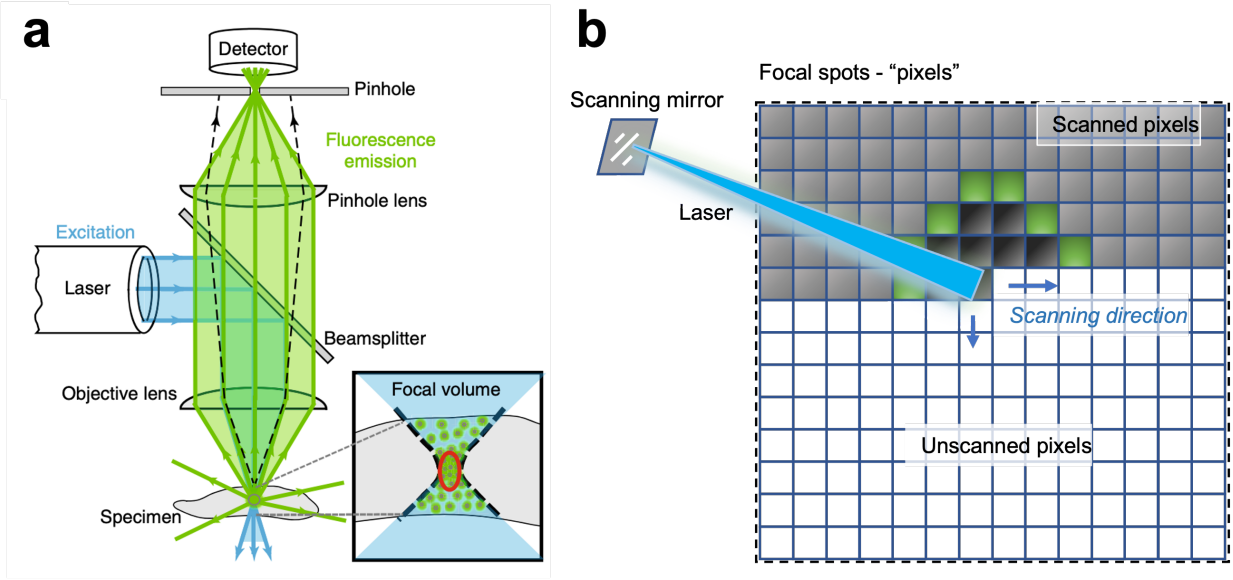

Figure 9: Illustration of the CLSM. The laser beam is focused onto the sample. Fluorescence emitted from the molecules in the focus (red oval) is directed to the detector through a pinhole. Black dashed line shows how light emitted from molecules outside of the focus does not reach the detector but is stopped by the pinhole. Figure reprinted from Jonkman et al[69]. b) Drawing illustrating the concept of laser scanning across a specimen in CLSMs (created with Inkscape[25]).

concept of confocal microscopy.

A confocal laser-scanning microscope (CLSM) uses a pinhole in order to block out-of-focus light from the detector (see figure 9a). A focused laser beam is passed to the sample to illuminate the fluorophores. The fluorescence (re-emitted light) is then collected via the objective lens and directed through a beam splitter to the pinhole lens. The pinhole is what allows for the high resolution in a CLSM image, as only light from the focal point of the laser will be directed by the pinhole lens through the pinhole. Thus only this light will reach the detector, and all other light from above and below the focus plane is simply blocked. Since only a tiny focal spot is collected by the laser, scanning mirrors are used to direct or 'scan' the beam across the entire sample to generate a complete image (see figure 9b). CLSMs can create optical sections < 1 µm, generating clear images of all layers in the sample without having to physically slice the sample. It is thus especially useful for determining the location, both in the lateral and axial direction, or co-localization of tagged molecules. The focused slices obtained can be used to create a 3D sample representation, by taking scans at different Z focus planes throughout the sample and stacking them on top of each other, creating what is known as a 3D z-stack. This of course requires that the 3D structures are preserved during sample preparation.

When using CLSMs, one needs to consider settings and drawbacks regarding the performance parameters for the instrument. As mentioned, the pinhole addition to the microscope reduces the size of detection and scanning is needed to generate a full image from combined sequential focal point pixels. This scanning introduces a disadvantage for CLSM as it puts a

time restrain on the image acquisition. When imaging live cells, it is critical that the image acquisition rate matches the speed of the dynamical process under investigation. Hence, imaging fast-moving objects with CLSM is not possible. Although the scanning rate can be adjusted independently, this affects the possible size of the image and reduces the quality - the inevitable trade-off in experimental microscopy.

The key to successful data acquisition is that you have the appropriate settings for the question at hand, as CLSMs can be optimized for different types of samples, depending on the desired outcome for the various performance parameters (see fig. 10). There is no need to prioritize high resolution if it is not particularly essential for the investigation. Higher resolution images are subject to other drawbacks such as longer acquisition time, larger data files, and the need to increase laser intensity which in turns increases the chance of photo-bleaching and toxicity[69]. Since settings such as laser intensity greatly affect the collected data, it is important to design an experiment thoroughly so that images are collected using the same settings if direct qualitative and quantitative comparisons are needed, for instance comparing fluorescent protein expression levels. In addition, image quality is not only determined by settings. Resolution is inversely proportional to wavelength, thus green or blue emitting dyes provide significantly better image resolution and contrast compared to red dyes, which have longer wavelengths[69].

Figure 10: Illustration of how a CLSM instrument can be optimized to be more or less suitable for a particular experiment. Here, the trade off for five key parameters are shown for contrast vs. live-cell imaging. Adapted from Jonkman et al[69].

3.2.1 Optical set-up

In this thesis, the set-up used to collect data combines the confocal microscopy technique described above with an optical trap. An optical trap consists of a highly focused laser which is used to trap objects and move them in 3D with nanometer precision. The concept and physics behind these traps, known as optical tweezers, is elaborated in the following section. In the optical set-up, the combination of the confocal microscope and optical trap allows for the probing and pulling of tethers from cell membranes, while simultaneously imaging the fluorescent signal from the NA or DiD-labelled membranes and elongated tethers. With this system, force profiles will be efficiently collected as immediate imaging reveals whether a tether was pulled or not.

The set-up uses a Leica SP5 CLSM combined with a 1064 nm Nd:YVO4 NIR laser (see figure 11). The trapping laser is expanded before it is directed to the sample and focused by a 63x water-immersion objective (NA 1.2) where after the laser light is collected by the

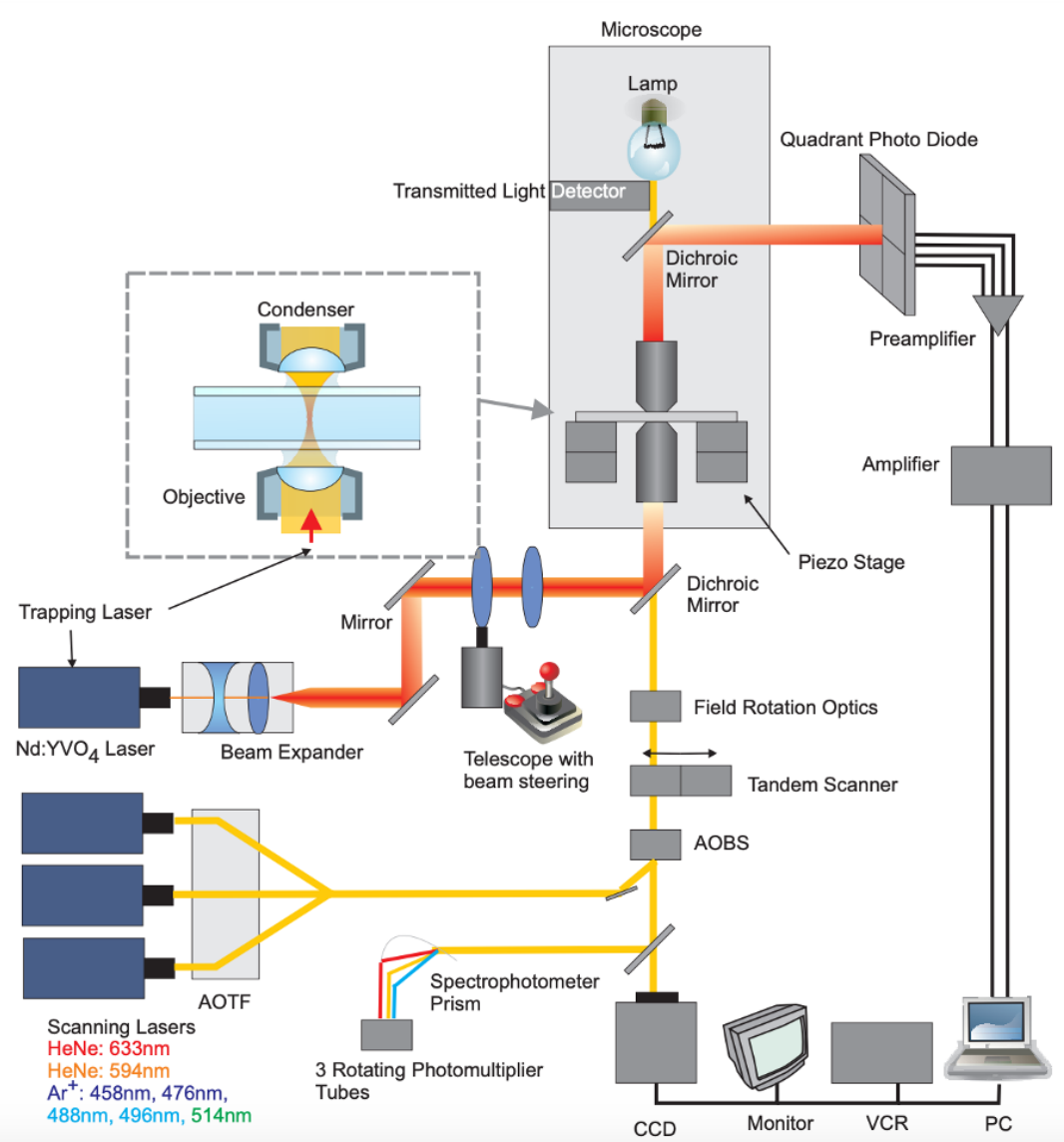

Figure 11: Schematic of the used set-up where a confocal microscope is combined with a 1064 nm optical trap. Reprinted from Richardson et al[70].

condenser (Oil immersion condenser, NA 1.4) and passed on to the quadrant photodiode, which records the information for the position and force detection of the trapped object[70]. The three scanning lasers in the system are passed through an AOTF, allowing for independent control, and then directed to the sample through the same objective lens (63x water-immersion objective, NA = 1.20) as the trapping laser. During experiments, a pinhole size of 111.4 µm were used and images of 512x512 pixels were scanned at 400 Hz. The scanning does not affect the optical trap as the set-up employs galvanic mirrors (tandem scanner) to move the scanning lasers (not the trapping laser) across the sample.

The confocal microscope, like all conventional microscopy, has a resolution limit given by the diffraction limit of the light. The lateral resolution of the microscope is generally described by the Rayleigh criterion and the minimum resolved distance defined as[61]

$$R_{confocal} = \frac{0.61 \cdot \lambda}{NA} \tag{1}$$

where λ is the wavelength of the incident laser and NA is the numeric aperture of the objective. In this project a 488 nm laser is used to image GFP-tagged NA and the numerical aperture of the 63x water immersion objective is 1.2. The minimum resolved distances that can be obtained are thus given as $R_{confocal} = \frac{0.61 \cdot 488 \text{ nm}}{1.2} = 248.07$ nm. Objects closer together cannot be distinguished as two separate objects. When multiple fluorophores are used on the sample, it is essential to avoid any spectral overlap, otherwise they will be indistinguishable in the detection. The spectra of the used fluorophores in this thesis can be found in the Supplementary information (SI), figure S30.

3.3 Optical tweezers

Optical tweezers (OTs) is a technique that utilizes a focused laser beam to manipulate and probe both microscopic and nanoscopic environments. The technique emerged with the construction of the first optical trap in 1970 by Arthur Ashkin[71] and have since been developed for use in numerous research fields, particularly to probe biological environments such as microorganisms and proteins. The technique is based on optical forces, creating a trap in which particles can be moved around with nanoscopic accuracy and forces in the piconewton range (0.1pN-200pN) can be either quantified or applied. This makes the tool extremely applicable for biological probing, since forces acting inside cells and between proteins are on this scale. The applications of optical tweezers are endless, as proven by the sheer abundance and diversity of systems probed and manipulated with this technique. It has been used to determine protein folding forces by pulling proteins apart with an optical trap on either end[72] and probe protein motors[73] such as kinesin, quantifying the inherent stepping length[74]. OTs have also been used simply to manipulate manipulating biological membranes via fusion from plasmonic heating or by pulling tethers from plasma membranes or vesicles[20,75]. In this project, the combined ability of the optical trap to pull and simultaneously measure the force on the trapped object, is exploited to quantify the force profiles of tubes pulled from various proteins embedded plasma membranes.

The theory behind trapping of particles in light depends on the size of the trapped object compared to the wavelength of the trapping light. Here I will describe the theory of trapping in the Mie (particle size larger than wavelength) and Rayleigh (particles smaller than wavelength) regimes, as the calculation of forces in the intermediate regime is non-trivial and outside the scope of this project. In addition, I will present methods used to calibrate an optical trap to allow quantitative measurement of the forces in the system.

3.3.1 Principles of trapping

In simple terms, the optical trap relies on the principle that light, consisting of photons, carries momentum. In a standard laser, the photons are distributed equally across the beam. In contrast, when the laser beam in an optical trap is focused, it creates a normal distribution of photons with the highest density in the middle of the beam. When light interacts with an object, the light is reflected or refracted. This interaction gives rise to two forces known as the scattering force and the refractive or so-called gradient force. The scattering force results from light being reflected and will push the object in the direction the photons are travelling. The gradient force comes from the refraction of light and will pull the object toward the center of the focused laser beam, when the refractive index of the object is higher than the surrounding media. It is therefore a *crucial* feature for optical trapping that the refractive index of the trapped item is larger than that of the sample environment. For this reason, silica or polystyrene beads are often used when the media is water since $n_{polyS} = 1.59 > n_{water} = 1.33$. Ultimately, to achieve stable trapping the gradient force must always exceed the scattering forces.

The theoretical mechanism of trapping can be explained using three distinct regimes that are based on the ratio of the beam wavelength λ to the diameter, d, of the trapped particle: The Mie regime where $\lambda < d$, the Rayleigh regime where $\lambda > d$, and the intermediate regime where $\lambda = d$. For the intermediate regime, the theoretical framework is extremely complicated, whereas the physics is comparably straightforward when discussing the extreme cases of trapping in the Rayleigh and Mie regimes.

The Rayleigh regime

The Rayleigh regime covers the situation in which the dimensions of the trapped object are much smaller than the wavelength of the incident light. The object thus experiences a constant field and can be treated as a dipole acting according to electromagnetic laws. A dielectric object in an electric field will be polarized by the incoming field $\mathbf{E}$ according to

$$\mathbf{d} = \alpha \mathbf{E} \tag{2}$$

where α is the polarizability of the object and $\mathbf{d}$ the induced dipole. The energy, stemming from the interaction of the dipole with the field, is given by

$$U = -\mathbf{d} \cdot \mathbf{E} \tag{3}$$

The force can then be derived from the potential energy gradient since $\mathbf{F} = -\boldsymbol{\nabla} U$ and is proportional to the gradient of the light intensity, I

$$\mathbf{F}_{grad} = -\boldsymbol{\nabla} U = -\boldsymbol{\nabla}(-\mathbf{d} \cdot \mathbf{E}) = -\boldsymbol{\nabla}(-\alpha \mathbf{E} \cdot \mathbf{E}) = \alpha \boldsymbol{\nabla} E^2 \tag{4}$$

$$\Rightarrow \mathbf{F}_{grad} \propto \alpha \boldsymbol{\nabla} I \tag{5}$$

This force is referred to as the gradient force and always points towards the maximum light intensity. For a focused laser beam, the light intensity profile is highest in the focal spot. Thus particles that come in contact with the laser will experience a pull towards the focal spot and ultimately get trapped in the center where the net force is zero.

In addition to the gradient force, two other forces act on the trapped object, contributing to the overall optical force; the scattering and absorption force, expressed as

$$F_{scat} = \frac{n \langle S \rangle}{c} \sigma_{scat} \tag{6}$$

$$F_{abs} = \frac{n \langle S \rangle}{c} \sigma_{abs} \tag{7}$$

where n is the index of refraction, σ_{scat} and σ_{abs} are the scattering and absorption cross sections of the object, c is the speed of light and $\langle S \rangle$ is the Poynting vector, representing the energy direction flux. These forces are a result of radiation pressure and act to displace the particle along the beam direction. Trapping in 3D requires that

$$F_{grad} > F_{scat} + F_{abs}. \tag{8}$$

Thus tightly focused laser beams are used to compensate for the scattering force and obtain stable trapping in the axial direction. Depending on the size of the scattering forces in the experiment, the object will be trapped slightly downstream of the focal spot.

The Mie regime

In the Mie regime, also known as the ray-optics regime, the trapping force can be explained and visualized using optic rays. The trapping becomes qualitatively explicit when following the momentum changes for the refracted light intensity beams.

When the object is positioned unevenly in the lateral direction of the trap, as in figure 12a, more photons are hitting one side of the particle (closer to the focal spot) than the other, due to the Gaussian shape of the laser beam. The refractive index of the object (always larger than the medium for trapping) causes a change in the direction of the momentum of the ray from p_1 to p_1'. As momentum is conserved, the object will have an equal momentum change in the opposite direction $-dp_1$. Due to the Gaussian distribution of the laser and consequent asymmetry of the ray intensities across the laterally displaced object, the object will experience a force towards the center of the beam, establishing stable lateral trapping.

To achieve axial trapping, the beam must be focused. Consider a trapped object placed slightly above the focal spot of the laser, see figure 12b. The refracted rays experience the momentum changes dp_1 and dp_2, and the resulting force on the particle pushes it towards

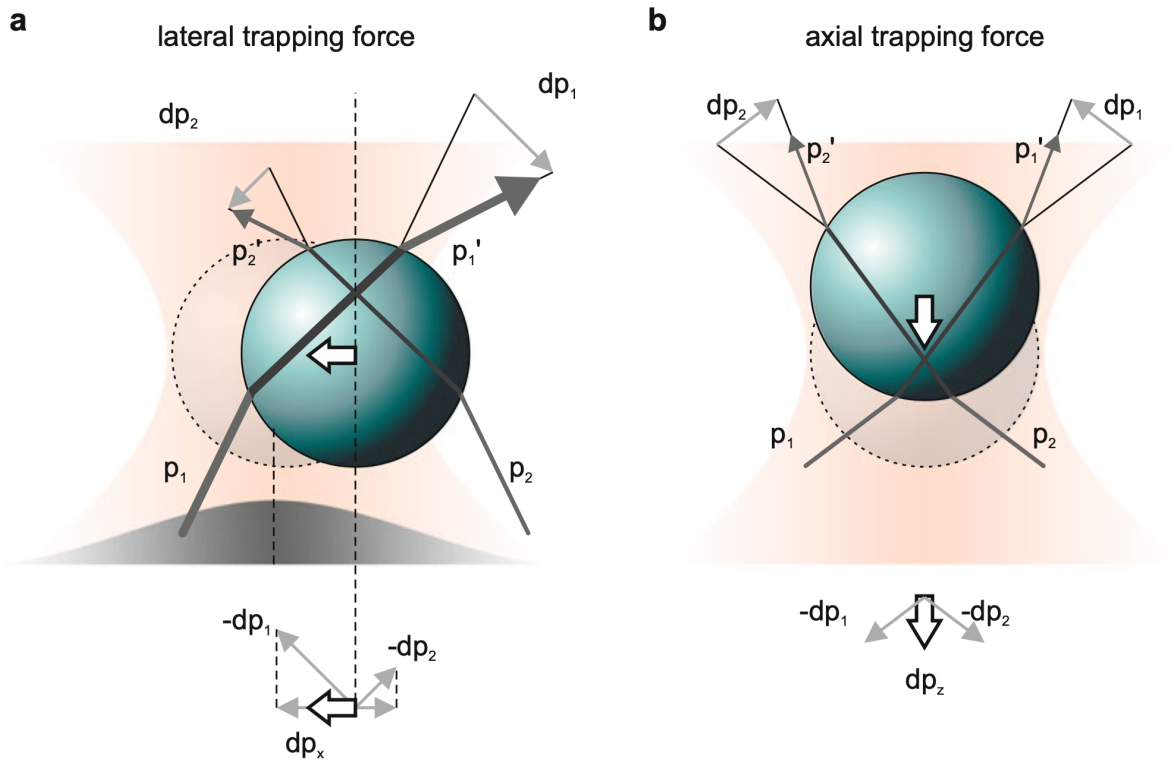

Figure 12: Forces on an optically trapped particle in the Mie regime. a) Lateral gradient force of a Gaussian laser beam profile. Lateral displacement of the object results in a change in momentum pushing it towards the center (white arrow). b) Axial gradient force towards the focus of the trapping light. Similarly, displacement causes a change in momentum resulting in the object being pushed to the axial focus point. The white arrows indicate the net restoring force. Reprinted from, Van Mameren et al[76].

the focal spot. This argument can be integrated over the entire laser profile to explain the trapping effect along the intensity gradient.

Often we are using particles that are somewhat in the middle of the Rayleigh and Mie regimes; the intermediate regime. In this project the particles trapped have dimensions d $\approx 5\mu$m, meaning we are on the borderline of intermediate and Mie regime. As the name indicates, this is where the wavelength is similar to the particle size, thus we cannot use either of the two simplifications above to describe this regime. Instead the electromagnetic theory regarding the interaction between matter and light can be applied to the system, however solving Maxwell's equations is not a trivial task in a case where size and geometry must be acknowledged[77,78]. In general, as it is inconvenient at best to theoretically calculate the optical forces exerted, the optical trap is instead calibrated to allow for direct force measurements.

3.3.2 Force calibration

As mentioned above, the forces in an optical trap are quantified by carrying out a force calibration. The trap can be modelled as a spring and thus the spring constant, or stiffness, can be used to quantify the force in the trap. The trap stiffness is often determined using either the Stokes drag calibration or the Brownian motion calibration analysis[76].

Stokes drag calibration

Consider a bead in an optical trap. The trap stiffness can be determined relatively easy by applying a constant external force to the bead and measuring its displacement in the trap. The constant external force is commonly created by applying a continuous fluid flow to the system or moving the trap with a constant speed. The drag force experienced due to the viscosity of the medium is described via Stokes' law

$$\mathbf{F}_{drag} = -\gamma \mathbf{v} \tag{9}$$

where $\mathbf{v}$ is the velocity vector and γ is the drag coefficient which is determined by the viscosity of the medium, η, and the diameter of the trapped bead, d, via $\gamma = 3\pi\eta d$. The drag force will displace the bead from the center until the force is equal and opposite to the trap restoring force given by Hooke's law

$$\mathbf{F}_{spring} = -\kappa \mathbf{x}. \tag{10}$$

The trap stiffness must therefore be

$$\kappa = \frac{\gamma \mathbf{v}}{\mathbf{x}}. \tag{11}$$

Hence, the stiffness can be calculated by measuring the displacement of a bead with a known diameter exposed to a fluid flow of known velocity and viscosity.

Brownian motion calibration

Brownian motion calibration is a more accurate method to determine the trap stiffness. It is based on the Brownian motion of the bead caused by the continuous stochastic force exerted on it by the surrounding solvent. From the Langevin equation of motion, the forces acting on the particle

$$m\mathbf{a} = -\kappa \mathbf{x} - \gamma \mathbf{v} + \mathcal{F}(\mathbf{T}, \mathbf{t}) \tag{12}$$

are the harmonic force of the trap, $-\kappa\mathbf{x}$, the drag force of the liquid medium, $-\gamma\mathbf{v}$, and $\mathcal{F}(\mathbf{T}, \mathbf{t})$, which is the stochastic force as a function of time and temperature of the medium. The stiffness in the trap can be found by taking the power spectrum of the bead. Using Fourier transformation, the power spectrums for the displacement fluctuations of the bead can be described as[79]

$$S_x(f) = \frac{k_B T}{\gamma \pi^2 (f_c^2 + f^2)}. \tag{13}$$

By fitting the power spectrum to the data, the corner frequency f_c can be extracted (see

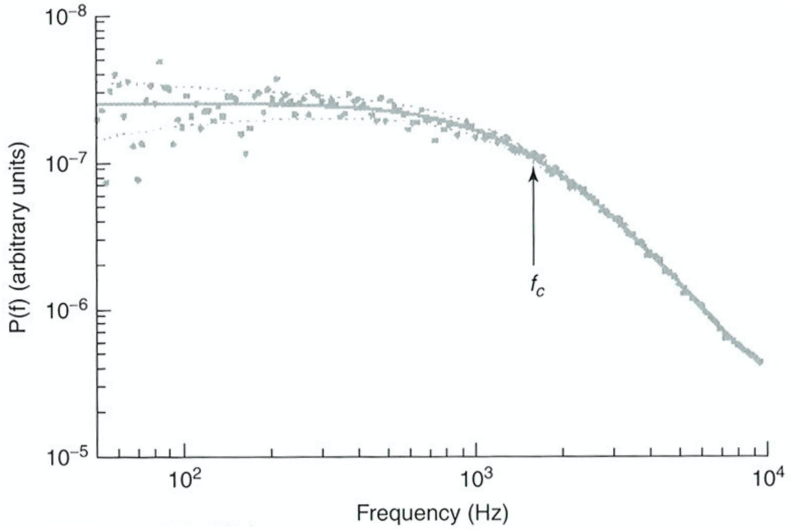

Figure 13: Example of a fitted power spectrum. The corner frequency, f_c is marked on the graph (arrow). Reprinted from Oddershede et al[78].

figure 13). Since the corner frequency is proportional to the trap stiffness by

$$f_c = \frac{\kappa}{2\pi\gamma}, \tag{14}$$

the force exerted by the trap can be calculated applying Eq. (10), when x is known.

3.4 Assessing the budding force using ultrasensitive optical trapping

Optical tweezers (OTs) are used in various ways to probe membranes and cells[20]. A common OT technique that has been extensively used to probe biological membranes is the pulling of nanotubes or 'tethers' from the plasma membrane surface[18–20]. *In vivo*, these membrane tethers are generated spontaneously and are vital parts of many biological processes in cells, including the extension of filopodia, endocytosis, cellular trafficking and intercellular nanotube connections[80–82]. By a applying a local point force, tethers can be artificially extracted from model membranes[83] or the plasma membrane[84], generating a useful assay for biophysical and mechanical investigations of membrane properties.

In practice, trapping a membrane-binding bead in an optic laser and establishing effective surface contact with the cell allows for pulling tethers from the membrane. When the membrane is pulled, a tube is formed with a radius and holding force characteristic of the mechanical properties of the given membrane. Therefore, the force measured from pulling-experiments can be used as an indicator of the membrane properties. In this project, we use the force generated to provide direct information regarding the membrane bending effect of crowding induced by the bulky viral spike proteins. The physics behind membrane bending and tether formation is described in the following.

3.4.1 Energy barrier for membrane bending

The membrane is a flexible barrier that can be deformed in various ways, however any deformation of the membrane is associated with a change in the free energy and thus requires the addition of energy to the system to overcome this inherent barrier. The membrane dynamics are classically described by the membrane tension and rigidity. As mentioned, a common method to study these membrane dynamics is by puling tethers from the cell surface. When pulling, a protrusion is first made from the membrane surface and the pulling force is then increased until the force barrier is broken. This results in transition of the protrusion to a tube[87], which then can be elongated. When imagining a piece of the membrane being attached to a bead at one point and being pulled straight out, one might intuitively expect the formation of a membrane extension into a cone-like shape. However, a narrow tether is formed instead due to the surface tension on the membrane. To minimize this tension the membrane surface is reduced to the minimum area configuration possible. The membrane attains this configuration by returning to its usual shape and the tube becoming, theoretically, infinitesimally thin. The forces of surface tension are however opposed by the rigidity of the membrane which fights the large curvature of an infinitely narrow tether. The result is a tether with a radius characterized by this balance of surface tension and bending rigidity[88]. The shape evolution of the tether formation is visualized in figure 14a.

The force and radius of the equilibrated membrane tube is related to the stretch and bending modulus of the specific membrane and can be described by minimizing the free energy of the system with respect to the length, L, and the radius, R, of the tether[86,88]. In model membranes (such as GUVs), assuming zero spontaneous curvature and an empty tube, the general relationship between the force, F, radius, R, and the mechanical parameters simplifies to

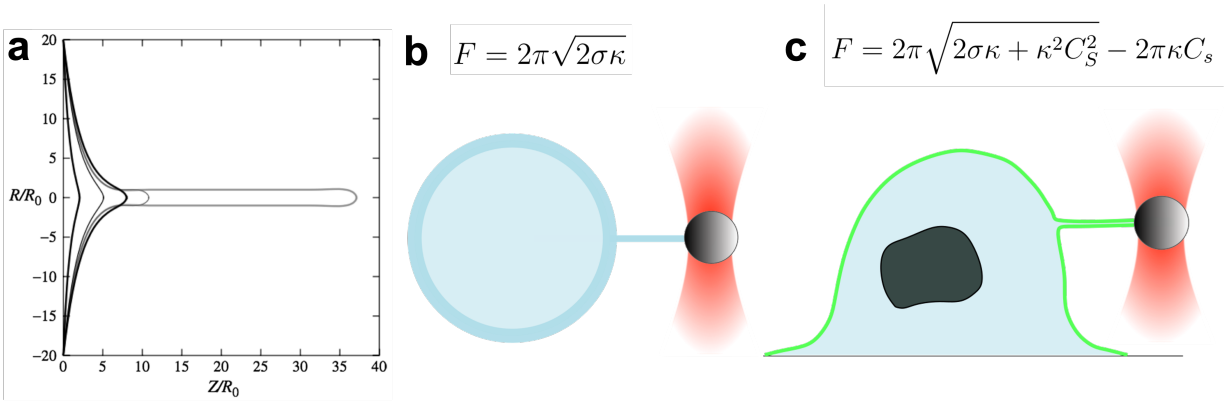

Figure 14: a) Computed tether shape evolution adapted from Derényi et al.[85] inspired by Nussenzveig[86]. The shape evolution illustrates the catenoidal tube conversion as a function of an applied force, F, for a circular patch defined with a radius, R_{ring}, and pulled to a "height" Z. b) Schematic of a tether pulled from a GUV. c) Schematic of tether pulled from a transfected cell (created using Inkscape[25]).

$$F = 2\pi\sqrt{2\sigma\kappa} \tag{15}$$

$$R = \sqrt{\frac{\kappa}{2\sigma}} \tag{16}$$

where σ is the membrane tension and κ is the bending rigidity (see figure 14b). These theoretical relations match well with experimental measurements[89,90]. From these two equations the relationship between the force and the tube radius can be described as

$$F = 4\pi\sigma R. \tag{17}$$

In experiments where the tension is kept constant, which can be done by sucking a vesicle into a micropipette[91], the force measurements can provide the tube radius of the tether. The radius can also be found by analyzing the intensity of fluorescent tags, and the two sets of values can be used to independently estimate the value of κ in the system[83].

When the membrane is pulled, the force profile reflects the change in membrane shape. However when pulling from cells instead of model membranes another contribution to the force profiles emerges: the effect of the cytoskeleton. The force curve of a tether pulled from a cell will show a linear rise in the force, reflecting the detachment and deformation of the spring-like cytoskeleton-membrane adhesion[92]. The applied pulling force must be able to overcome this adhesion energy barrier in order to pull a tether from the membrane. When the cytoskeleton detaches, the force drops abruptly before reaching a plateau. Finally, when the pull is stopped, the force will relax exponentially to equilibrium.

When a protein is introduced into the membrane of a cell the force relationship changes and is now also dependent on the spontaneous curvature provided by the protein (see figure 14c). When minimizing the free energy again, the force can now be described as

$$F = 2\pi\sqrt{2\sigma\kappa + \kappa^2 C_s^2} - 2\pi\kappa C_s \tag{18}$$

where C_s is the spontaneous curvature[21]. Many membrane proteins are involved in membrane fission, and the energy needed to break the energetic barrier of fission is predicted to lie in the range of 400-800 k_BT[93]. Thus a significant energy contribution must be provided by proteins involved in membrane fission, if they must facilitate breaking this barrier[14].

In this thesis, tethers with lengths of 5-10 µm are extracted from the plasma membrane of NA transfected HEK cells by 5 µm membrane-binding beads in an optical trap (see figure 14c). The tether pulling force profiles are then compared between native and NA-crowded cell membranes. The binding area between the bead and the surface is not controlled in the set-up. Thus, the force barriers (peak forces) are not comparable for the pulls, instead the equilibrium tether forces are compared to quantify the effect of NA-induced crowding on membrane mechanics and spontaneous curvature.

4 Materials and Methods

Here all materials and methods are presented in a concise manner.

4.1 Cell culture specifications

Human embryonic kidney 293 cells with mutant version of SV40 large T antigen (referred to as HEK in the thesis). Gibco™ Dulbecco's Modified Eagle Medium, High Glucose. Gibco™ Fetal Bovine Serum. Gibco™ Penicillin-Streptomycin. CTS™ TrypLE™ Select Enzyme. Gibco™ Trypsin-EDTA (0.05%), Phenol red Invitrogen. PBS Phosphate-Buffered Saline 10X pH 7.4. Lipofectamine™ LTX Reagent with PLUS™ Reagent. Thermo Scientific Nunc™ Cell-Culture Treated Multidishes 6 (9.6cm2) well. Invitrogen™ Molecular Probes™ Vybrant™ DiD Cell-Labeling Solution. Gibco™ FluoroBrite™ DMEM.

4.2 Experimental specifications

Menzel-Gläser Cover slips (24 x 60 mm #1.5). Menzel-Gläser High precision Microscope Cover Glasses (22 x 22 mm No. 1.5H, 170 μm). The beads used were 4.9 µm (diameter) Streptavidin Coated Polystyrene Microspheres from Bangs laboratories Ink, 10mg microspheres/mL (1% solids w/v). Chamber silicone template were made from SYLGARD 186 silicone based elastomeric kit, forming a PDMS composite (Sigma-Aldrich).

4.3 Cell culture

Frozen HEK293T cell vials were thawed in a water bath at 37°C. The cryomedium was removed and replaced with fresh 37°C culture medium seeded in T25 culture flasks and cultured at 37C and 5% CO2 (standard cellular conditions). The culture medium used consisted of Dulbecco's Modified Eagle Medium (DMEM) supplemented with 10% Fetal Bovine Serum and 1% Penicillin-Streptomycin. The cells were passaged upon 70-90% confluency and cultured at maximum until passage 19. Passaging occurred every 2-5 days, depending on conditions. Cells were washed with 2 ml phosphate-buffered saline (PBS), incubated with 0.5 ml Trypsin-EDTA for 2-5 min to allow detachment, then spun down, resuspended in 8 ml fresh medium and 1/5 of the cell solution transferred to a new cell flask with 3 ml medium. Upon splitting, the cell concentration of suspended cells was determined by staining with Trypan Blue and analyzed in an Invitrogen Countess Automated Cell Counter. Cells were then seeded in 6-well plates for experimental use.

4.4 Membrane labelling with DiD

The day prior to labelling, 4-800.000 HEK cells were seeded in 6-well plates with 2 ml medium. A DiD labelling solution was made by diluting 4 μl DiD in 1 mL culture medium.

The medium in the well was removed and replaced with the DiD solution, where after the cells were incubated 10 min. at 37°C and 5% CO2. The solution was then removed and the cells washed twice with PBS. The cells were then detached with TrypLE and seeded in a chamber for experiments.

4.5 Transfection

Transfection is a technique used to artificially introduce foreign DNA or RNA into cells, allowing for e.g. the expression of various engineered proteins. Several chemical and physical methods have been developed for transfections. The chosen method for this project was the common cationic lipid-mediated transient transfection using Lipofectamine LTX. This method allows for efficient transportation of the chosen plasmids across the plasma membrane, where the plasmids are released into the cytosol via the endocytic pathway.

The transfection solution was made by mixing 1.5 μg plasmid with 3 μl PLUS reagent in an Eppendorf tube containing 75 μl opti-MEM. In addition, 3 μl Lipofectamine LXT was diluted in 75 μl opti-MEM and the two solution were left to incubate for 5 min, where after they were mixed and incubated another 30 min. The day prior to transfection, 4-800.000 HEK293T cells were seeded in 6-well plates with 2 ml medium in order to obtain ca. 60% confluency after 24 hours. Upon transfection, the medium was then removed, and the cells washed using 1 ml PBS. 2 ml opti-MEM was added to the well and the freshly made transfection solution deposited evenly around the well. After 3 hours of incubation at 37C and 5% CO2, the transfection medium was replaced with culture medium. The cells were then left at 37°C and 5% CO2 another 24 hours reaching 80-90% confluency for experiments.

4.6 Chamber design and preparation

In this project, successful experimental data consists of both clear fluorescence imaging of tethers pulled from the plasma membrane and a clear force profile for the entire pull. Achieving the optimal conditions for experimental success required a well-designed and balanced sample preparation set-up. In the chamber design, considerations were made regarding; the ability to optically trap beads, the health of the cells, and the timeslot for successful data collection.

In order to collect the force profile from the bead, a chamber with a top and bottom seal were needed. A completely enclosed chamber, using a top and bottom cover glass slip around a PDMS template, was chosen as it allowed for continuous measurements without media evaporation. However, the streptavidin coated polystyrene beads used here, experience non-specific binding with uncoated glass slides, resulting in the majority of the beads sticking non-reversibly to the glass slide almost immediately upon reaching the bottom. Protein coated glass-slides is a common way to prevent this electrostatic interaction, how-

ever coating also interferes with cellular surface receptors and lowers the cells' ability to adhere to the glass – a feature that is critical for pulling experiments. To avoid surface adsorption of the beads, the sample cover slide was passivated with the mammalian milk protein β-casein. β-casein binds strongly to a SiO_2 surface and is therefore an effective and commonly used inhibitor of surface adsorption[94,95]. A low concentration (0.1%) of β-casein, provided the conditions for excellent data collection, allowing cells to adhere while keeping the beads in solution (trappable) for up to 1.5-2 hours.

Cleaning the slides:
Unwanted microscopic impurities on the cover slips can disturb image collection, add uncertainty to the experimental data or even have a toxic impact on the live cells in the experiment. To remove impurities the chamber slides are cleaned before use. Cover slips (24x60 #1.5 and 22x22 No. 1.5H) were placed in a solution of 96% ethanol and sonicated for 30-60 min. This step was repeated 3 times and the slides were then left in a fresh ethanol solution until use.

Coating chamber bottom with β-casein:
The chamber was created by cutting out templates from a thin PDMS layer. The template was rinsed in ethanol, dried and stuck to the center of a bottom cover slip. A solution of (0.1%) β-casein in TRIS buffer was added to the chamber and incubated for 5 min. The solution was removed, the chamber rinsed twice with PBS and then dried for $>$ 10 min.

Seeding cells in the chamber:
A low concentration of cells was seeded in the chamber in a solution of FluoroBrite DMEM, which is used to enhance fluorescence imaging. The chamber was placed in an incubator for 30-45 min, allowing the cells time to adhere slightly to the glass slide. 10 µl of a 2:1000 PBS dilution of beads (from stock, see specifications) was then dropped into the chamber. After 10 min the beads started to appear on the bottom surface, easily trapped.

4.7 Force analysis

4.7.1 Experimental platform and settings

The chamber was mounted on the set-up via a sample holder. A 63x water immersion objective (NA 1.2) was used in the microscope and a ca. 30 µl droplet of water placed between the cover slip and the objective. An Oil condenser (NA 1.4) was added to the microscope and an oil droplet added on top of the chamber before the condenser was lowered to connect with the oil and top cover glass. The aperture of the microscope was fully opened at 24 and the light intensity was minimized. The argon laser was used at 20% intensity. Standard settings for confocal image collection was set for the three types of samples (HEK,

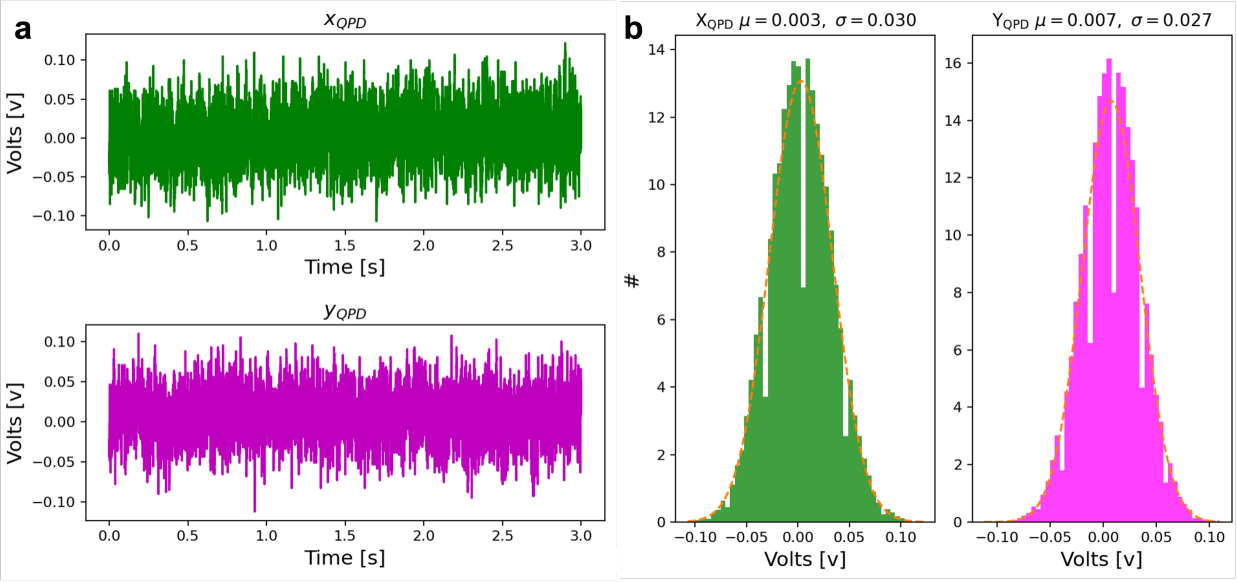

Figure 15: a) Example of raw QPD signal (V) in X and Y for a calibration file. b) Position histograms of raw signal with fitted Gaussian distributions and associated σ printed. Graphs created using python lumicks.pylake package.

NA-transfected HEK, DiD-labelled HEK) (see SI, section 8.2). The current through the trapping laser diode was kept constant at 9A for all experiments.

4.7.2 Force calibration and unit conversion

For every pull a 5 µm bead was first trapped in the laser. The bead was lifted from the glass surface (3-8 µm) and moved into an empty area near a cell of interest for the analysis of the thermal fluctuations. Three force calibration curves were then obtained for the bead, collecting 66000 scans of the QPD voltage signal for the X and Y position using a 22kHz scanning frequency. This calibration was done for every new bead trapped during experiments.

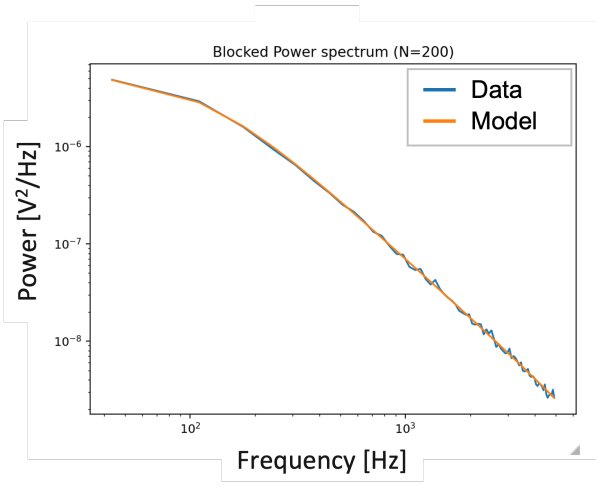

Figure 16: Example of a fitted power spectrum with the lumick.pylake package. Model is fitted to the thermal fluctuation data of a trapped bead.

The calibration curve was used to extract the conversion factor translating the QPD signals from voltage to force. The initial signal was recorded by a quadrant photodiode in volts (V) (see figure 15a). Using a free dedicated python package[96] (lumicks.pylake), a histogram plot of the bead position fluctuations signal (V) in X and Y is plotted, determining the standard deviation and subsequently the conversion factor (see figure 15b). In addition, a power spectrum was fitted to the X and Y position (see figure 16)

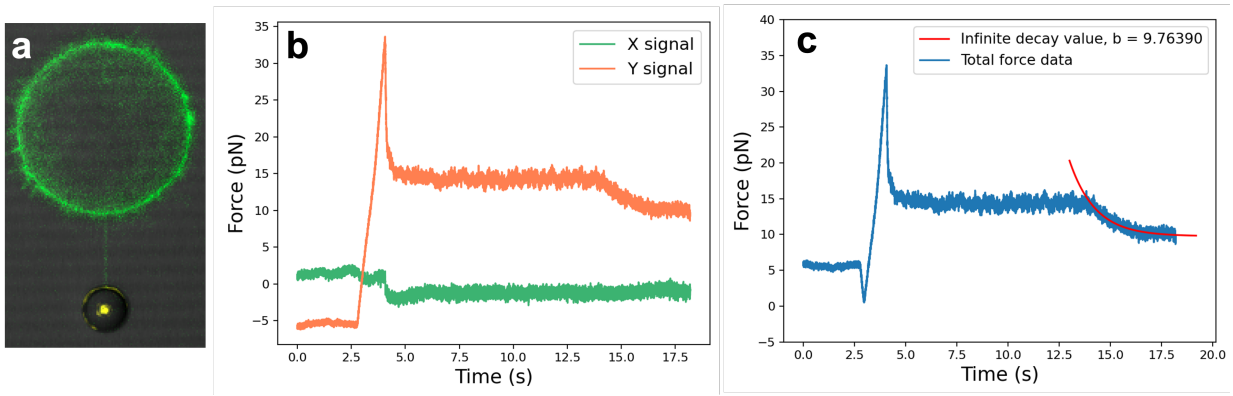

Figure 17: Tether equilibrium force extraction. a) Overlay image of GFP fluorescent signal (green) from an NA-transfected HEK cell with an elongated tether held by a trapped bead. b) Corresponding force trace for the X and Y signals. c) Total force for the pull. Exponential function is fitted from relaxation initiation at ca. 14 s. and is indicated with a red line. The obtained infinite decay value is b = 9.76390 pN.

to get the corner frequency. In practice the python program fitted the data and returned the mean force response, Rf (pN/V), value for the X and Y signal which was subsequently used to translate the pull force profiles into force (pN) vs. time (s) (see figure 17 for example).

4.7.3 Tether equilibrium force extraction

When pulling a tether from a cell (see figure 17a) a force is applied to the membrane resulting in the formation of a tube with radius related to the tension and bending rigidity as described in section 3.4. The force to pull the tether is measured from the bead displacement in the trap and the bead position and the resulting tether is tracked by confocal microscopy live imaging.

The conversion factor for the X and Y position was extracted from the data as described above. The conversion factors for the X and Y position were then used to convert the X and Y pull signal from voltage to force, respectively (see figure 17b). The total force profile was then calculated using the Pythagorean theorem

$$F_{tot} = \sqrt{F_x^2 + F_y^2} \tag{19}$$

where F_x and F_y are the force profiles in the X and Y direction respectively on the QPD. To get the equilibrium force of the tether from the data, an exponential function was fitted to the relaxation curve (see figure 17c). The relaxation starts from the moment the pull is stopped. A manual estimation of the pull stop time was made and the subsequent data points where included in the exponential fit to extract the infinite decay value. If the relaxation was disrupted by tether snapping or similarly after relaxation, then these deviating data points were excluded from the fit (see SI, figure S32). In addition, data points where either two tethers were visible or the force exceeded 30 pN were excluded from analysis (see section 5.1.5).

4.8 Statistical analysis of tether forces

The significance of the distinct sample population means for plasma membrane equilibrium forces was evaluated statistically in Prism[97]. The data was first checked and confirmed to be normally distributed in 4/4 completed normality tests (Anderson-Darling, D'Agostino & Pearson, Shapiro-Wilk and Kolmogorov-Smirnov test), see SI, figure S33 for details. A one-way analysis of variance (ANOVA) test was carried out assuming Gaussian distribution but not assuming equal variance (Welch ANOVA test). A multiple comparisons test was selected, comparing the mean of each group with the mean of every other group in the data (Dunnett's 3T multiple comparisons test).

4.9 Data processing tools

Fluorescence analysis of tube and membrane intensity was conducted using the open-source image analysis software Fiji[98]. Generel data analysis and graph generation was done in the Python programming language[99], utilizing Jupyter Notebook[100]. Calibration of the optical trap was done by employing the lumicks.pylake force calibration package in Python[96]. Statistical analysis of data was done in GraphPad Prism[97]. Schematic drawings and figures were created with Inkscape[25]. Boxplots were made using the web tool BoxPlotR[101].

5 Results and discussion

5.1 Experimental set-up allows for effective data collection

In this first section of the results and discussion, the data collection and analysis process is reviewed and validated to emphasize the applicability of the results obtained in the study. Tethers are pulled from three types of membranes in this thesis: 1) Native, non-transfected HEK cells, 2) HEK cells incubated with the fluorescent membrane dye DiD and 3) NA-transfected HEK cells. These groups will be referred to as ”Control”, ”DiD” and ”NA” in the following.

5.1.1 Lipophilic dye and fluorescent proteins ensure visibility of cells

NA is an influenza A virus protein and is thus not endogenously expressed in HEK cells. DNA plasmids must therefore be introduced into the cell via transfection, to allow for the expression of NA. To be able to follow the protein expression level and visualize the pulled membrane tethers, the protein is tagged with GFP. Not surprisingly, the transfection is only partially successful (see figure 18a) as seen by the many non-fluorescent HEK cells in the sample. This is attributed to the transfection technique and the fact that NA is a large transmembrane protein which needs to be synthesized and transported to the plasma membrane. However, this amount of transfection is perfectly acceptable for the experiments in question as it is possible to perform the experiments in transfected single cells within the sample. As expected, the fluorescently tagged NA protein is predominantly localized in the plasma membrane. However patches of green fluorescence are visible inside the cells, which could be the origin of synthetization (the endoplasmic reticulum) of NA, before its transportation to the plasma membrane.

The control cells (simply non-transfected HEK cells) were either used in experiments

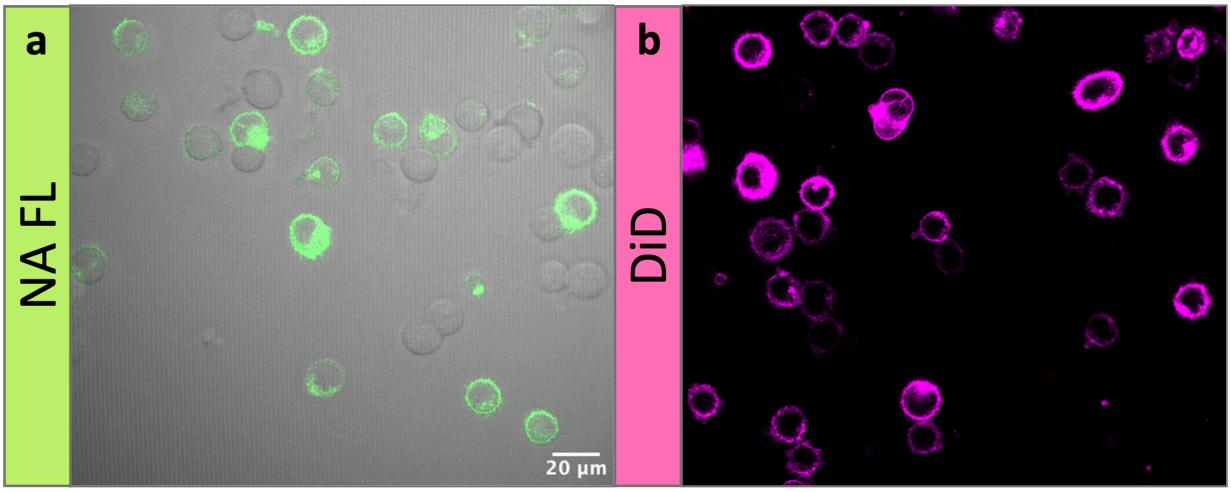

Figure 18: Fluorescent signals from cells. a) HEK cells transfected with GFP-tagged NA. b) HEK cells labelled with membrane dye (DiD).

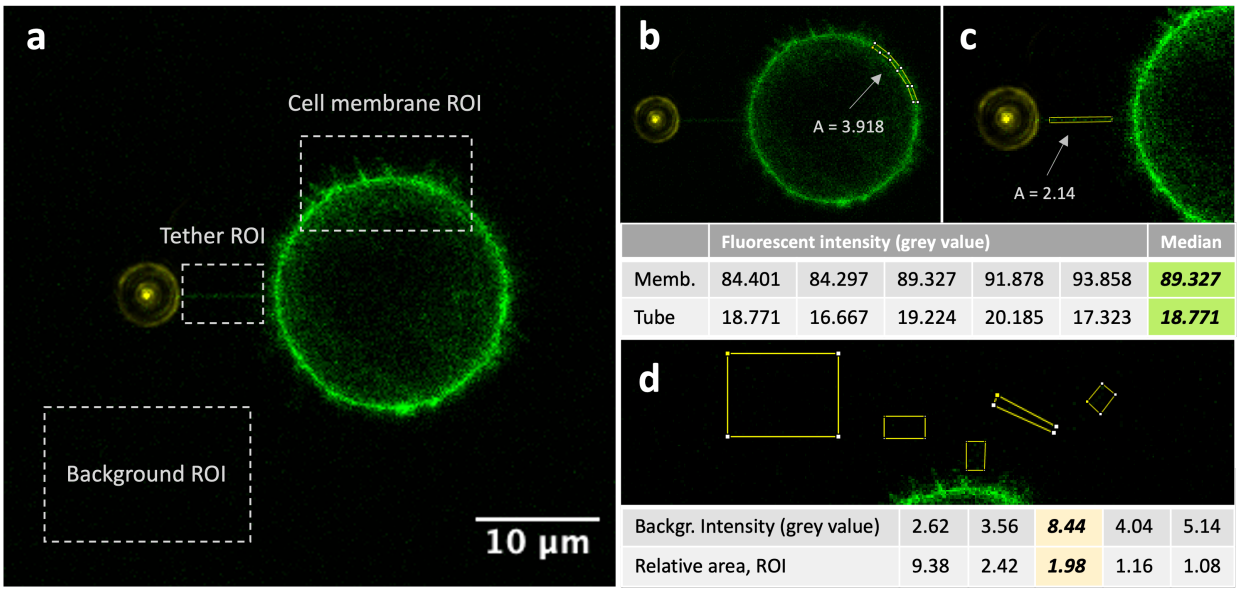

	Fluorescent intensity (grey value)					Median
Memb.	84.401	84.297	89.327	91.878	93.858	***89.327***
Tube	18.771	16.667	19.224	20.185	17.323	***18.771***

d

Backgr. Intensity (grey value)	2.62	3.56	***8.44***	4.04	5.14
Relative area, ROI	9.38	2.42	***1.98***	1.16	1.08

Figure 19: Fluorescent signal analysis. a) Regions of interest (ROI): The background, the tether and the membrane signal. b) Marked membrane region illustrating how the average membrane signal (proportional to protein coverage) is obtained. c) Tether intensity is determined by a narrow marking. Example values for membrane and tube intensity is listed below. For each pull, the median of five markings was recorded and used in further data analysis. d) Background markings of various area sizes (au) and corresponding intensities indicate bias of tube intensities below 9.

without any fluorescent membrane tags, or were incubated with DiD before imaging. Over time, DiD is internalized in the cell, therefore they are imaged shortly after DiD incubation. Although all cells appear to be labelled, the cell membranes are not labelled with DiD to the same extent (figure 18b).

5.1.2 Fluorescence analysis shows variance in membrane coverage and tube radius

In the pulling experiments, the fluorescence signal of the membrane and tether is used to extract data pertaining to membrane crowding of NA. The cells showed clear expression of NA (see figure 19a) and DiD in the membrane and tethers.

The membrane protein coverage was determined relatively from cell to cell using fluorescent intensity analysis. A section of the membrane was marked using a masking tool in Fiji (figure 19b). The chosen section excluded the membrane part where the tether was formed. Instead an area was chosen with a similar intensity profile as that from which the pull was initiated. The average grey value for this selection was measured and recorded (figure 19b). This selection process was completed 5 times and the resulting median value was used in all further analysis of the membrane coverage for the pull. In addition to the membrane intensity, the tube intensity was similarly determined by taking the median of 5 consecutive, narrow selections of the tube (figure 19c). For the NA-transfected cells, the membrane was not subjected to the membrane dye DiD, so the relative tube radius was determined solely from the intensity of NA. This GFP-tagged full length neuraminidase

(see figure 5b for reference) protein is a suitable membrane marker as it has been shown to not be curvature sensitive[12], meaning it does not tend to upconcentrate in tubes and skew the data. Therefore the relative tube radii of the NA pulls are expected to relay similar intensity values as would have been obtained from a membrane marker e.g. DiD.

The fluorescent intensities measured in this thesis is only used to compare data points within the same group *relative* to each other. Therefore the background is not subtracted from the measured intensity. However, as shown in figure 19d the background provides a biased readout for the fluorescence intensity of the tethers. Depending on the placement and area of the background measurement, different values can be obtained. Example areas and placements of background measurements (figure 19d, bottom) indicate the bias that exists in the tube intensity data, as a grey value of 8.44 was obtained for an area (au) measurement of similar size to a tether measurement. Thus tether intensities under 9 are assumed biased in this study. Consequently, these data points have been removed from the presented data to minimize uncertainties.

Fluorescence intensity analysis provides information regarding the protein expression, which can be compared internally for each experiment type and is denoted as the relative membrane coverage in this thesis. The distributions of NA expression and DiD binding to the membrane is shown in figure 20a,b. The level of protein expression varies from cell to cell, thus it is expected that the data shows a wide range of membrane protein coverage. This can depend on the uptake of plasmid DNA by the cell and how effectively the protein is synthesized and transported to the membrane. Often transfection is limited by the transportation of the viral plasmid across the plasma membrane and degradation inside the cytosol. For the purpose of analyzing how crowding impacts the budding force, it is ideal to be able to compare cells of different protein coverage levels. Thus, here the wide variety of NA expression provides an advantage in data collection. The incorporation of DiD into the cell membrane also varies depending on the incubation time and concentration of DiD in vicinity of the cell, and the analyzed cells present different DiD levels. As the microscope settings and the fluorophores are different for NA and DiD, it is important to highlight that the relative membrane coverage cannot be directly compared. The actual % fluorescent molecules on the surface can be calculated by finding the appropriate conversion factors for the fluorophores in question. In addition to membrane coverage indications, the fluorescent signal also relays information regarding the radius of the pulled tether. Generally the radius of a tether is given by

$$R_{tub} = K_{tub}\frac{I_{tub}}{I_{mem}} \tag{20}$$

where R_{tub} is the tether radius, I_{tub} is the average fluorescent intensity in the tether, I_{mem} is the average fluorescent intensity of the membrane and K_{tub} is a calibration factor relating the fluorescence signal to the actual distance in nm[83]. Here the calibration factor has not

been determined for the instrumental set-up, thus the relative tube radius within the groups are used in the analysis. The membranes of the control HEK cells are not labelled, thus the distribution of tether radii acquired in these pulls are unknown, and it is not evident whether the tether size distribution is comparable to that of NA (see figure 20c). However, since the DiD tethers also show a large relative radius size distribution (figure 20d), it is expected that similar variance is also present for the control cells.

The fact that the radius of tethers pulled from the HEK cells incubated with DiD varies greatly indicates that the membrane tension and bending rigidity is not constant even for cells in the same population. This is not a surprise as the cell is a very complex system and many parameters can vary from cell to cell and influence the plasma membrane interactions. Thus, this initial analysis could be an indication of the difficulty in comparing the crowding effect on live HEK cells.

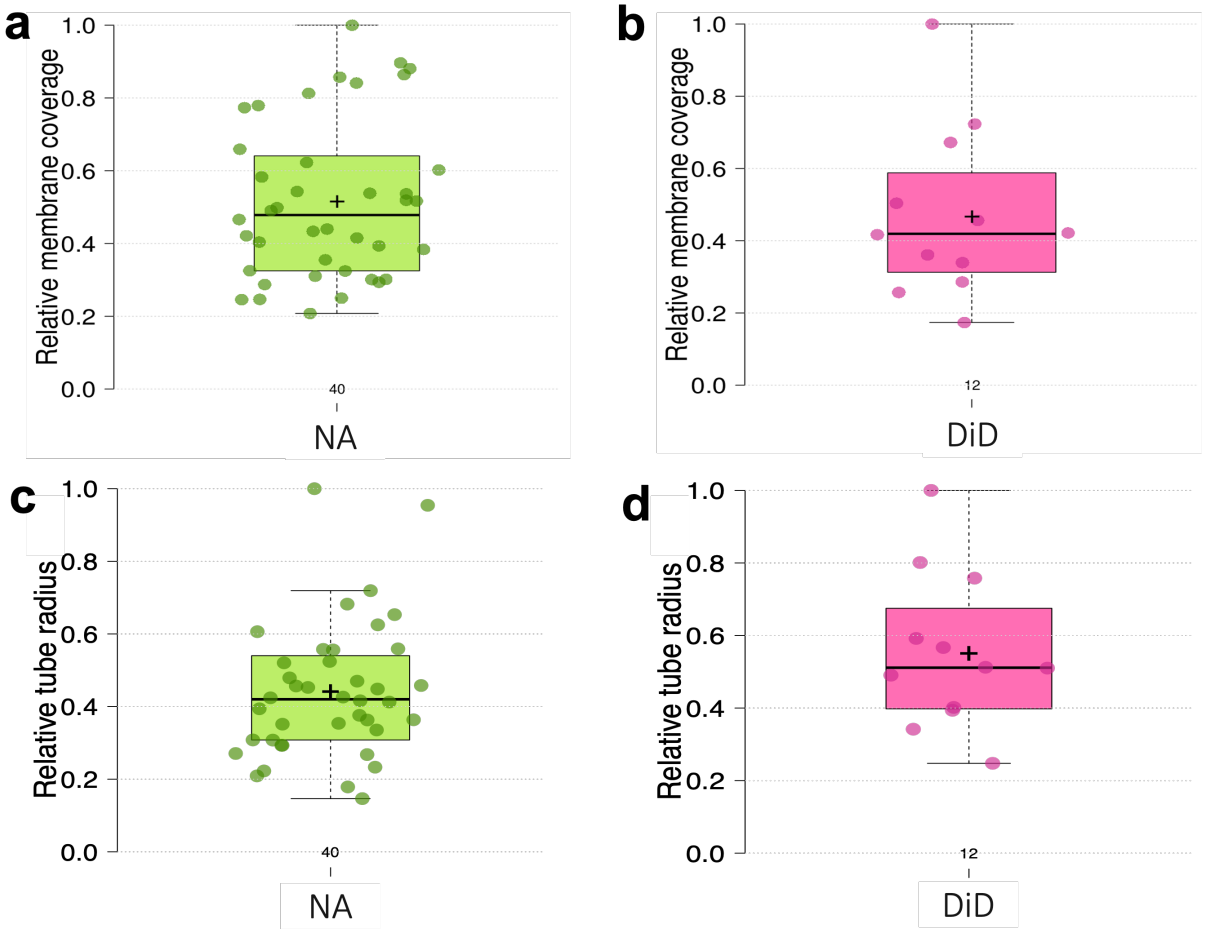

Figure 20: Distribution of DiD and NA expression in membranes and tethers. a) and b) Jittered boxplots showing the distributions of the relative membrane coverage by NA expression and DiD membrane-binding respectively. c) and d) Jittered boxplots showing the distributions of the relative tube radius of NA-transfected and DiD-labelled cells respectively. Whiskers extend to data points that are less than 1.5 x IQR away from 1st/3rdquartile. Plots were made using the web tool BoxPlotR[101]. Note: one cannot directly compare the relative tube radii for the two types of cells, as the settings and fluorophores are different for the data.

5.1.3 Experimental force traces follow theoretical shape

In this thesis, HEK cells were transfected and seeded in a glass chamber together with streptavidin-coated polystyrene beads (5 µm). The beads were trapped in a focused laser and subsequently used to pull tethers from cell membranes. The protrusion-to-tether transition, the so-called crossover, had a success rate of around 40% for pulling of 5-10 µm tethers. Often, unsuccessful pulls were completed. Either the bead did not adhere properly to the surface and no initiation of pull was observed, the bead-to-surface grip on the adhesion patch was abruptly lost or the elongated tether snapped before the completion of the pull. This could indicate that the unspecific binding of streptavidin-coated beads to the membrane surface is not perfectly effective and that the membrane bending force in these cases is larger than the attraction force between the bead and the membrane surface. Occasionally, the tether nucleation force exceeds the trapping force in the optical tweezer. If the bead sticks tightly to the plasma membrane, it will then be lost from the trap during the pull and adhere to the cell. This can happen if the bead adheres to a large surface patch, as the force will increase with the patch size[87].

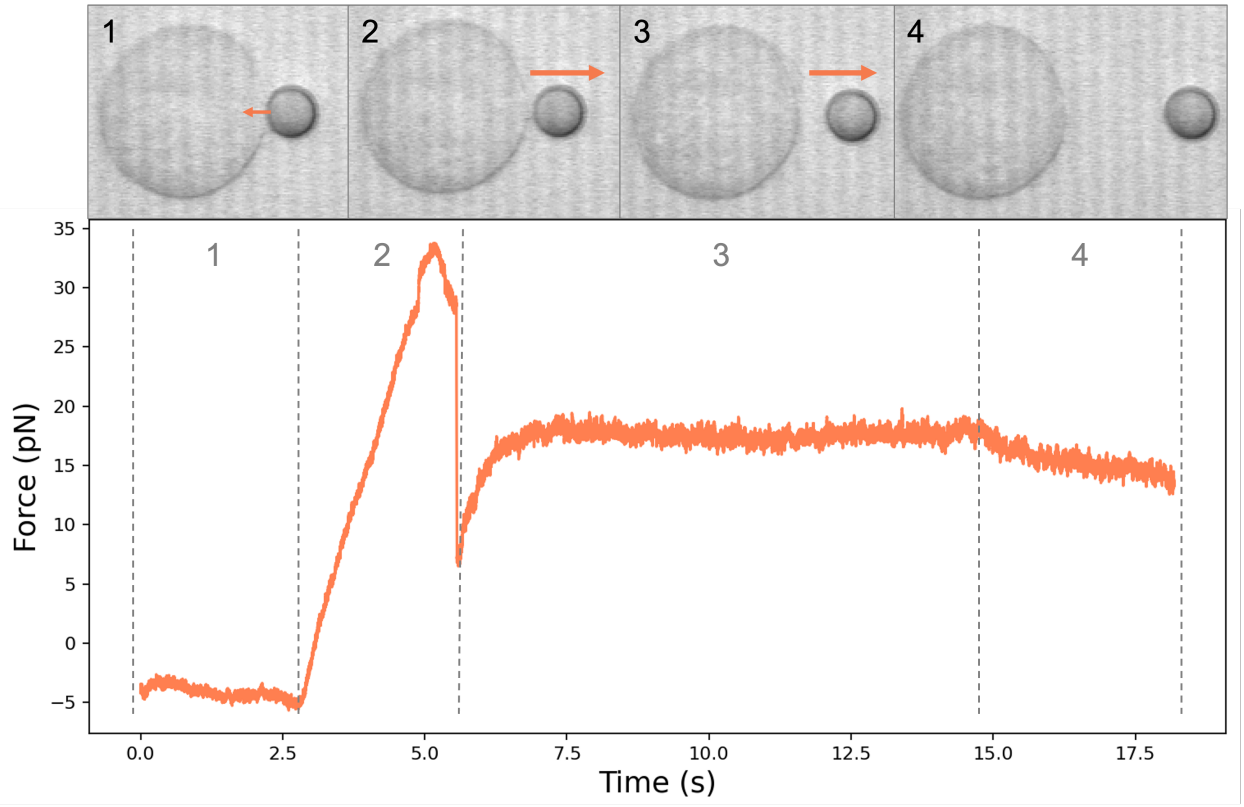

Figure 21: Force footprint from tether pulling with corresponding cell images reflecting the stages of the pulling experiment. The trace can be described by 4 regimes. 1: Impingement of bead against cell surface to establish adhesion, which displaces the bead from the trap center resulting in a negative force. 2: Tether nucleation (crossover) occurs at the 6s mark where the force goes down, whereas the linear increase is the deformation of the actin cortex (like a spring force). When the force goes down and the tether nucleates the membrane simultaneously detaches from the actin cortex and the cortex is allowed to bounce back. 3: Tether elongation, where the force drops immediately upon crossover and increases slightly during elongation. 4: Tether relaxation i.e. re-distribution of membrane lipids until equilibrium is obtained.

The recorded force profiles for the tether pulls vary in shape (see SI, figure S31), however the general pull can be split into 4 regimes: 1) Impingement, 2) Nucleation, 3) Elongation and 4) Relaxation. These four sections explain the force trace, and are further detailed in figure 21. The force recording is initiated after the bead is pushed against the cell membrane, and ends after allowing the tether time to relax. Successful pulls require minimum interference from objects in solution, e.g. secreted vesicles, or interaction between the bead and glass surface.

5.1.4 Equilibrium forces are extracted from relaxed tethers

In order to compare the forces between different tether pulls, the tether must be elongated and allowed to relax to its equilibrium position[88]. This tether 'holding' force can then be compared for each pull data set. The membrane tension of course has a huge impact on the tether nucleation force, however the force peak is not reliably comparable between the experiments as the force and radius of the resulting tether depends on the contact area of the bead and the cell surface[86,87]. This variable is not controlled for in this experimental set-up, thus the equilibrium tether force is used in the analysis. The equilibrium force is determined by fitting an exponential decay function to the relaxation part of the pull curve (see figure 22). The tether elongation was terminated after around 14 s. and tether lengths varied from 5-10 µm. Allowing the tether time to fully relax provides a more accurate measurement for the holding force. In later parts of the thesis, a longer collection time was adopted to allow for this (see figure 22a and b), however partial relaxation data, obtained in a few experiments, is included in the analysis and discussion, as the exponential fit provides a suitable indication of the equilibrium force.

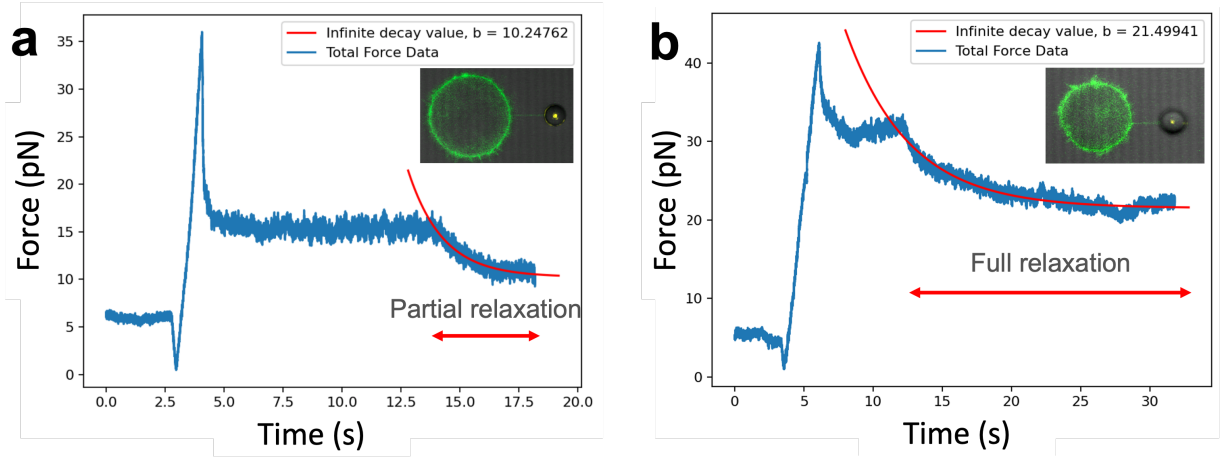

Figure 22: Force traces for pulling experiments with a) "partial" relaxation, where the tether is allowed to relax for ca. 4 s. or b) "full" relaxation, where relaxation is achieved over ca. 18 s. Exponential fit is indicated with a red line. Inserts show the obtained tether.

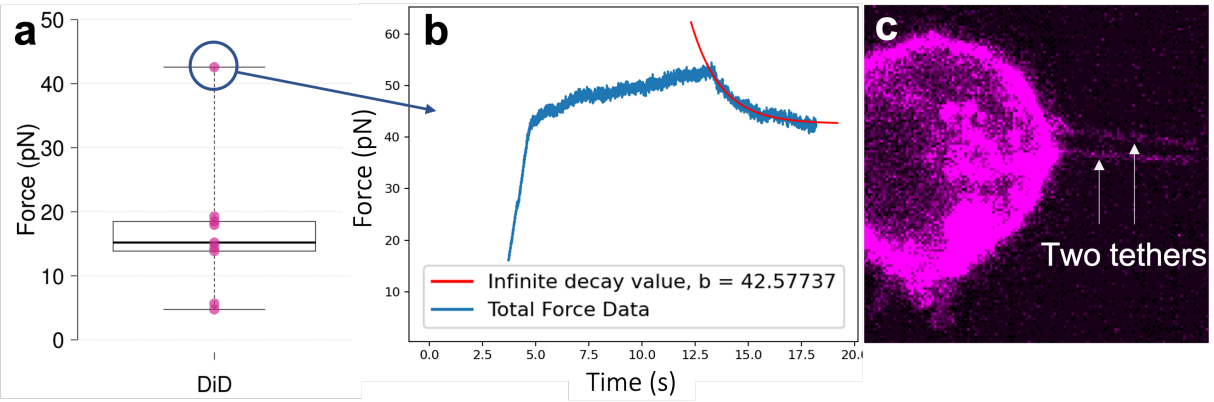

Figure 23: Double tether data. a) Boxplot of DiD data with outlier data point for a double-tether pull at 42.6 pN. Whiskers extend to minimum and maximum values. b) Force trace of outlier point with fitted exponential. The force of 42.6 pN is more than double the force of the rest of the pulled tethers. c) Confocal image of DiD-labelled HEK cell with two tethers pulled simultaneously (see arrows). The DiD signal is over-saturated to better visualize the tethers.

5.1.5 Features of pulling experiments

Pulling tethers from cell membranes is not a simple task. The plasma membrane is a complex system and various phenomena can materialize in the pulling data. During data collection, numerous archetypical features were observed in the data. Correct interpretation of these features is key to relevant data analysis. Here two traditional features are shown in detail.

Although tethers tend to coalesce[102] in model membranes, it is possible to pull two tethers simultaneously from the plasma membrane of cells. This is a result of the bead attaching at two points on the membrane surface upon impingement. These double pulls were largely, clearly visible in the confocal microscope and a distinct subpopulation of 'outliers' in the force boxplots at around 30-45 pN were observed (figure 23a). Naturally, the inclusion of such double tether pulls will skew the population mean of the tether forces. Therefore all pulls where either two tethers were visible or the force exceeded 30 pN (often both were the case) were excluded from the data analysis. Previously, the mean equilibrium force for tethers pulled from HEK293 (similar to the HEK293T cells used here) have been found to be higher (39 pN) than the results in this thesis, however, as confocal images confirm double tethers, the exclusion of data points > 30 pN in this set-up is appropriate.

In addition, some force traces exhibit sharp, instantaneous drops in the force (see figure 24a) at various points during the pulls (see additional example in SI, figure S32). These drops vary in size but often lie in the 15-20 pN range. Two events that can explain the occurrences of these drops are the "snapping" or "merging" of tethers (see figure 24b). When two tethers are pulled simultaneously with distinct adhesion points on the bead, it is possible that one -or more- of these extra tethers snap during the pull. This is similar to when a single tether is lost during elongation. In addition, as mentioned above, merging or coalescence of tethers can happen[102]. Whether snapping or merging is the explanation for the drop in force, both

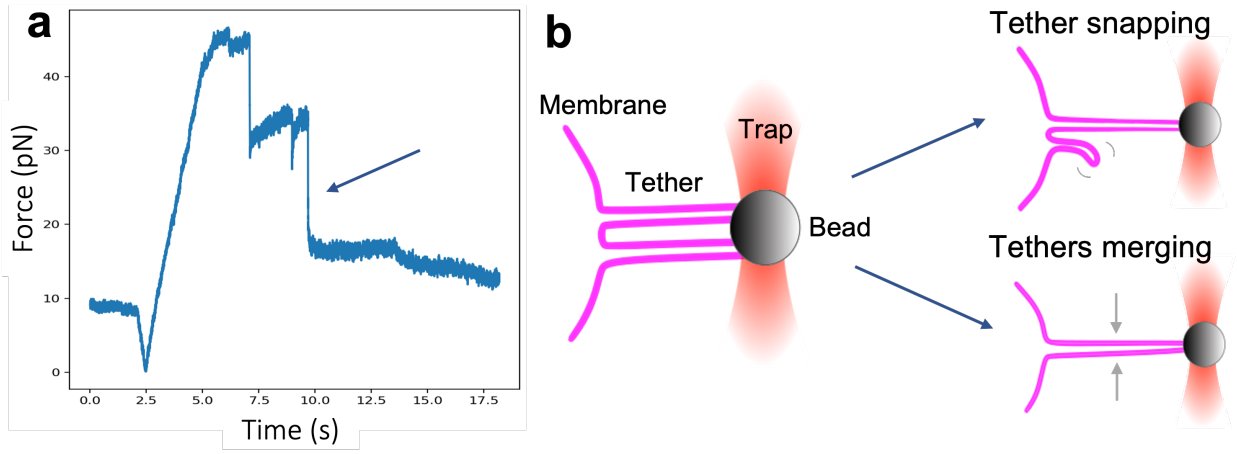

Figure 24: Illustrating scenarios explaining observed sharp, force drops. a) Force profile containing a large force drop (arrow). b) Schematic drawing of double tethers pulled by a trapped bead (left). The possible scenarios for the sharp force drops, resulting in a single tether, are the snapping of a tether (top right) or the merging of the two tethers to one (bottom right). The pink lines represent a membrane with DiD dye. Created with Inkscape[25].

result in only a single tether being held by the bead. Therefore, the corresponding force curves are completely valid to use as long as a tether relaxation is obtained at the end of the pull.

5.2 Masking effect of membrane mechanics on NA crowding

In this part of the thesis, the forces from transfected cells will be compared to the force from control cells, as well as cells labelled with the membrane dye DiD. This analysis provides information regarding the ability of NA crowding to induce spontaneous curvature of the cell membrane from crowding, possibly rendering the membrane more malleable compared to control cells.

The tether equilibrium forces obtained from the pulling experiments show a significant difference (p-value < 0.0001) between the sample mean of tethers pulled from NA-transfected cells compared to control cells (see figure 25). The mean force for control cells was 10.95 pN compared to 17.47 pN for NA cells. Thus the data shows that holding tethers pulled from an NA-crowded membrane requires a higher force. In contrast, the differences between the control vs. DiD group and the NA vs. DiD group are not significant (p-value of 0.5361 and 0.2661 respectively). The obtained data was segmented based on tube intensity analysis (see section 5.1.2 for details), meaning that data points representing pulls where the tether intensity was below a set threshold value have been excluded from the presented data. The statistical analysis was, however, confirmed to yield similar results if all data points would have been included (see SI, figure S34b). Data points obtained using partial and full relaxation experimental protocol were treated as one group as the means were found to not be significantly different (p-value = 0.2175), and thus the data is taken to originate from

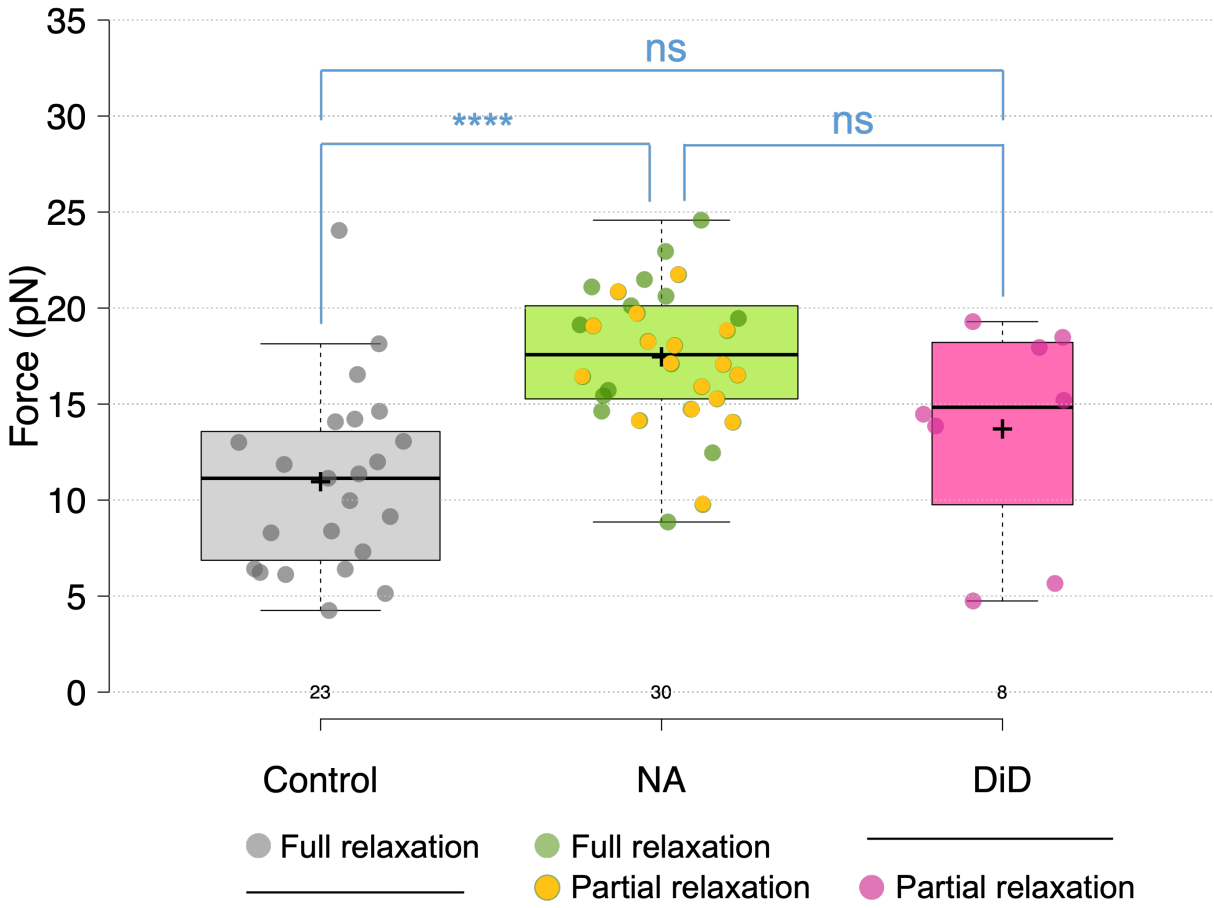

Figure 25: Jittered boxplot of equilibrium tether force values for the three groups: control (HEK cells) with 23 data points, NA (NA transfected HEK cells) with 30 data points and DiD (DiD incubated HEK cells) with 8 data points. Whiskers extend to data points that are less than 1.5 x IQR away from 1st/3rd quartile. The sample means are: control = 10.95 pN, NA = 17.47 pN, DiD = 13.71 pN. The control group and NA is significantly different with an adjusted p-value < 0.0001. Control vs. DiD and NA vs. DiD is not significantly different (ns) with adjusted p-value of 0.5361 and 0.2661, respectively. Full and partial relaxation is specified with colors (see section 5.1.4 for explanation). Figure created using web-tool BoxPlotR[101].

the same distribution (see SI, figure S34a). Data was first checked and confirmed to be normally distributed and the significance levels were obtained from a one-way ANOVA test (see section 4.8 for details).

The observant reader will notice that the number of data points in each group varies considerably. This is due to multiple reasons: 1) the nature of the experimental set-up and 2) procedural changes made during the thesis. When pulling tethers from cell membranes, numerous factors determine data outcome. An example of such a factor is the ease of obtaining and elongating a tether which in turn depends on the force barrier and the bead-to-surface adhesion. The particular cells from which pulling is attempted also have an influence and as mentioned previously only around 40% of pulls resulted in tether formation. This could explain some of the within-group variance in the data. In addition, different amounts of pulls were excluded from analysis for each group due to discrepancies i.e. multiple tethers,

inadequate tube intensity or inconclusive equilibrium forces. A change in the relaxation time was made from ca. 4 to ca. 18 seconds, in order to make sure the true equilibrium value was reached, hence the indication of partial and full relaxation in figure 25. Simultaneously, a switch from DiD cells to controls cells without a membrane marker was made, explaining the lack of full relaxation as well as number of data points for the DiD group.

The change away from DiD incubated cells was made to avoid any influences of DiD on the membrane properties. DiD is a lipophillic membrane dye used in order to image and analyze tubes pulled from the cells. One can imagine that the incorporation of the molecules in the membrane can have an effect on the mechanical properties and thus the pull forces, however whether this is actually the case is not known. Bouvrais et al. demonstrated that similar dyes (e.g. DiL) have an effect on membrane properties at certain high concentrations, however these were higher than normally used in fluorescence imaging[103]. Thus, it is unlikely that there is a large effect on the membrane rigidity from DiD. Still, the force varies a lot even with the few data points obtained for DiD (figure 25) and the difference between NA and DiD is not significant. Hence, while it is not completely clear from the few data points analyzed, there might be some effect of DiD on the equilibrium force of the membrane tethers, and any such effect would not be present in the NA-transfected cells. Thus a switch to wildtype HEK cells (control) were made, as tethers could still be verified from the 'snapping back' of the bead upon release from the trap. The DiD data was used as a means to portray the variance in tube radii for non-transfected cells (figure 20d) and provides basis for assuming similar variance for the unlabelled control cells. Alternatively DiD could be used in the NA group as well, providing the same basis for comparison between the NA and DiD groups. However, it is still better to completely avoid any possible effects from membrane incorporation of DiD by employing the native HEK control group.

In conclusion, there is a clear difference between the mean force in the control group and the NA group, indicating that the force needed to pull tethers from the transfected cells is larger. Our hypothesis was that NA-crowding lowers the energy barrier for membrane budding and consequently also for tether formation. Hence, this result is puzzling. In general the tether equilibrium force is given by

$$F = 2\pi\sqrt{2\sigma\kappa + \kappa^2 C_S^2} - 2\pi\kappa C_s \tag{21}$$

where σ is the tension, κ is the bending ridigity and C_s is the spontaneous curvature (see section 3.4.1 for details). The addition of the proteins are postulated to affect the C_s value in the equation as they would provide spontaneous curvature to the membrane. Thus an increase in C_s is predicted to decrease the force needed to hold a tether (see figure 26a). However, this is not observed in the data (figure 25).

It is possible that NA crowding does in fact increase spontaneous curvature, but that the effect is hidden by an effect on other variables as well. For example, if the tension

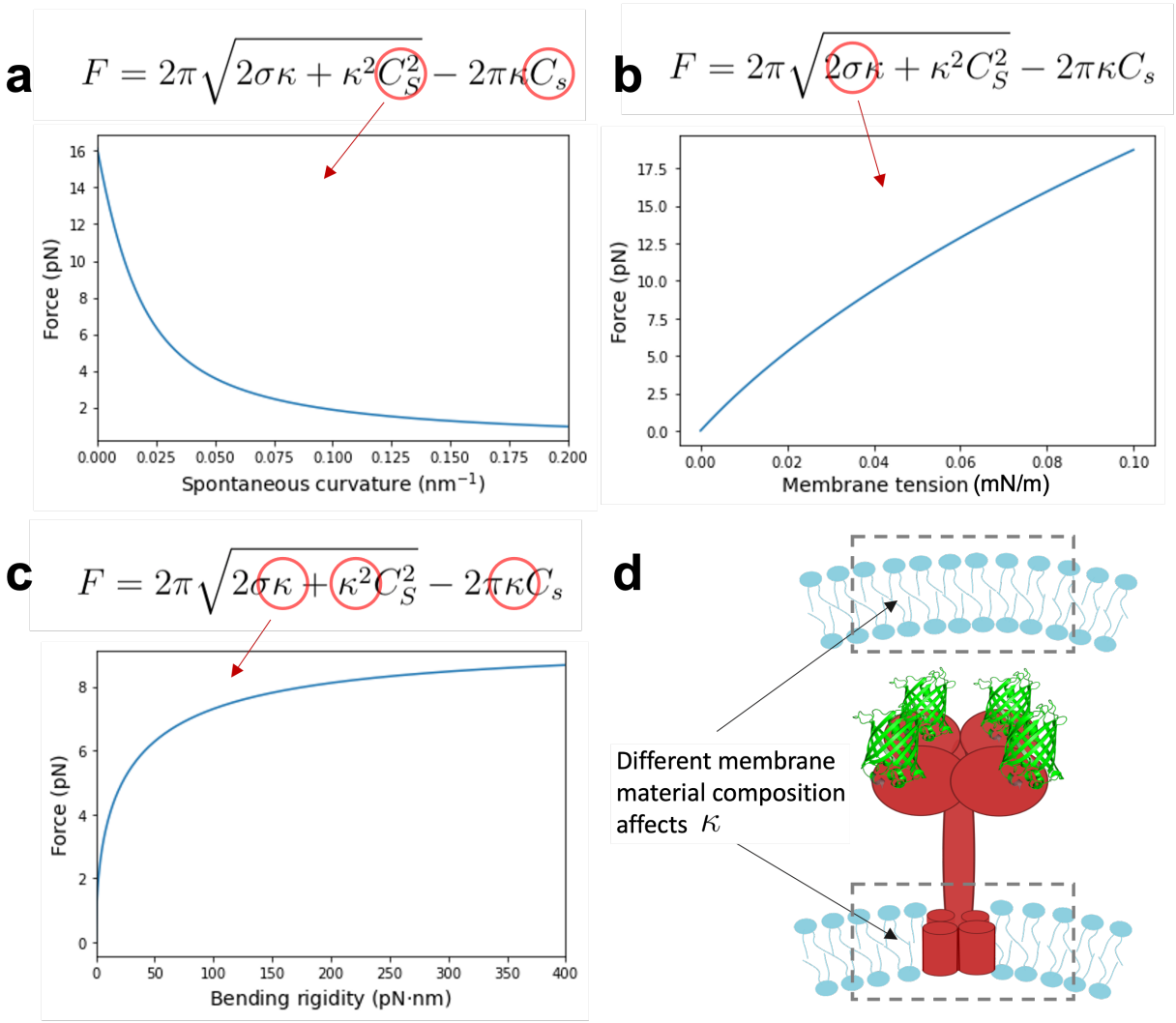

Figure 26: Tether equilibrium force dependence on variables. Plots are generated with the following values: $\kappa = 110.0$ pN $\cdot$ nm, $\sigma = 0.03$ mN/m, $C_s = 0.02$ nm^{-1} inspired by literature[21]. a) The force decreases as a function of spontaneous curvature. b) The force increases as a function of membrane tension. c) The force increases as a function of bending rigidity. d) Schematic of the change in membrane material composition of a lipid bilayer (top) upon insertion of the transmembrane domain of NA (bottom). Created with Inkscape[25].

for the transfected cells is larger than for the control cells, this larger σ could overshadow the effect of the NA protein (see figure 26b). In this context, it is worth noting that a bias exists in the set-up in regards to the membrane of HEK cells, namely the transfection process. Transfection via lipofectamine is in itself a process in which the membrane is subjected to a high concentration of reagents which induce the delivery of DNA plasmids to the cell. As the non-transfected cells are not subjected to this treatment, it introduces another point of uncertainty. The control cells could be subjected to this treatment without the addition of DNA plasmids to eliminate such bias. In addition, the membrane rigidity could also be affected by the insertion of NA into the membrane (figure 26c,d), as explored in the following section. Finally, the structure of the spike protein might not be as effective as hypothesized. Crowding of proteins can provide the steric pressure needed to facilitate membrane bending, however, studies show that small ordered domains drive bending less

effectively than intrinsically disordered protein (IDP) domains[14]. Since the viral proteins are ordered domains, it is plausible that they do not exhibit crowding on as large a scale as assumed in this thesis. It is thus possible that the set-up does not provide the necessary conditions to observe a crowding effect. Below, it is discussed in detail how membrane mechanics of the transfected cells might mask the effect of crowding on equilibrium force measurements.

5.2.1 Transmembrane insertions affects the rigidity of the membrane

When NA is expressed in the cell, a large transmembrane domain (TMD) sits in the plasma membrane (see figure 26d). This insertion of the TMD changes the composition of the bilayer and thus the interaction between the lipids and proteins that make up the plasma membrane. Essentially the 'material' is being changed, which means its properties are likely also affected. Such an alteration is reflected in the membrane rigidity (κ) that is characteristic for a certain membrane (figure 26c). Dimova et al. reviews studies of membrane bending rigidity alterations by membrane insertions and summarizes how both stiffening and softening can occur depending on the nature of the inserted proteins and lipids[104]. Proteins that are not intrinsically shaped to promote curvature, but are rather stiff with a cylindrical TMD can contribute to an effective increase in the bending rigidity, as has been discussed for aquaporin in relation to membrane protein sorting[105]. In addition, data is even available on how the membrane bending rigidity can be affected by different fluorescent labels commonly used to visualize membrane domains[103]. The softening and stiffening observed for protein insertions into membranes has led to the development of models which characterize this effect. Such models postulate that proteins have unique mechanical signatures that are dictated by their coupling with the surrounding lipids in the membrane[106].

In membrane pulling-experiments, the equilibrium tether force depends on the rigidity of the membrane and increases as κ increases (see figure 26c). If the transient expression of NA in the membrane results in an increase in κ, it could mask any spontaneous curvature effect from crowding. As the membrane rigidity has been shown to change with the insertion of proteins before[104,107], it is very plausible that expression of NA in HEK cell membranes changes κ. Whether this change would increase or decrease the bending rigidity is however uncertain and should be determined experimentally. In contrast to the artificial overexpression of NA in the HEK cell membranes, much less viral protein is expressed during infection *in vivo*. Thus, NA expression by infected cells could still increase spontaneous curvature without affecting membrane rigidity to the same extent as surmised here.

5.2.2 The role of the actin cortex

The actin cortex, also referred to as the actin cytoskeleton, is a network of cytoplasmic proteins that lies on the inner face of -and is tethered to- the plasma membrane. The actin

cortex is responsible for the linear increase in the force during pulls, until it detaches from the membrane (see figure 21). Ideally, the length of the tube should have no effect on the holding force as long as the membrane tension is kept constant. However, there is a limit to this theory when the tethers are pulled rapidly[108] - the force increases when the membrane reservoir runs out. It is postulated that the existence of a reservoir-limit arises from the failure of the the actin skeleton to remodel accordingly and release membrane sections during rapid pulls. The integrity of this actin cytoskeleton contributes to the mechanical parameters of the cells[109], and the membrane tension can diverge among different regions of the same cell[92]. Thus it is difficult to control for variations in the tension during experiments, and the variance of forces measured could very well be attributed to this effect. In addition, the role of membrane cortex linkers on membrane tether equilibrium forces has been investigated, indicating that the force required to pull a tether increases with expression of the examined cortex linkers[110].

Indeed many factors determine the membrane tension of a specific cell. If the actin-membrane interaction changes upon NA expression, it could result in an increased tension compared to control cells and thereby explain the observed increase in force (figure 25). Whether the effect would be on the overall tension in the membrane or manifest via some additional interaction of actin inside the tethers can be considered.

It has also been shown that actin can be present in tethers and that the tether force changes depending on the actin activity and the cell type investigated[111,112]. However, compared to these studies, the time interval during which the force is measured in this thesis is too short for the actin cytoskeleton to have an effect. However, it has also been demonstrated that actin is always present in tethers when extrusion occurs at filopodial speed[113]. Thus it is plausible that extra linkage is created between the actin cortex and the overexpressed NA proteins, consequently increasing the membrane tension, or that the force is affected by a difference in interaction of the actin cytoskeleton with the tethers. Investigating the crowding affect of NA using model membranes, and hence removing the potential effects of the actin cortex, could provide interesting details on this matter.

5.3 Increasing NA coverage reveals crowding effect

In this section of the thesis NA-transfected cells are examined in detail. The impact of protein coverage on the equilibrium force is investigated by comparing cells with various amounts of NA expression. According to literature[14,52,53,55], the force should decrease with increasing protein coverage if a dominant crowding effect is at play here.

In figure 27a the force vs. relative membrane coverage is shown. As membrane coverage increases, we see a trend towards decreasing equilibrium force. This trend is further visualized by lines which connect the mean force in each bin of width 0.25 (see figure 27a). The data shows a slight increase from bin 1 going to 3, however only two data points are

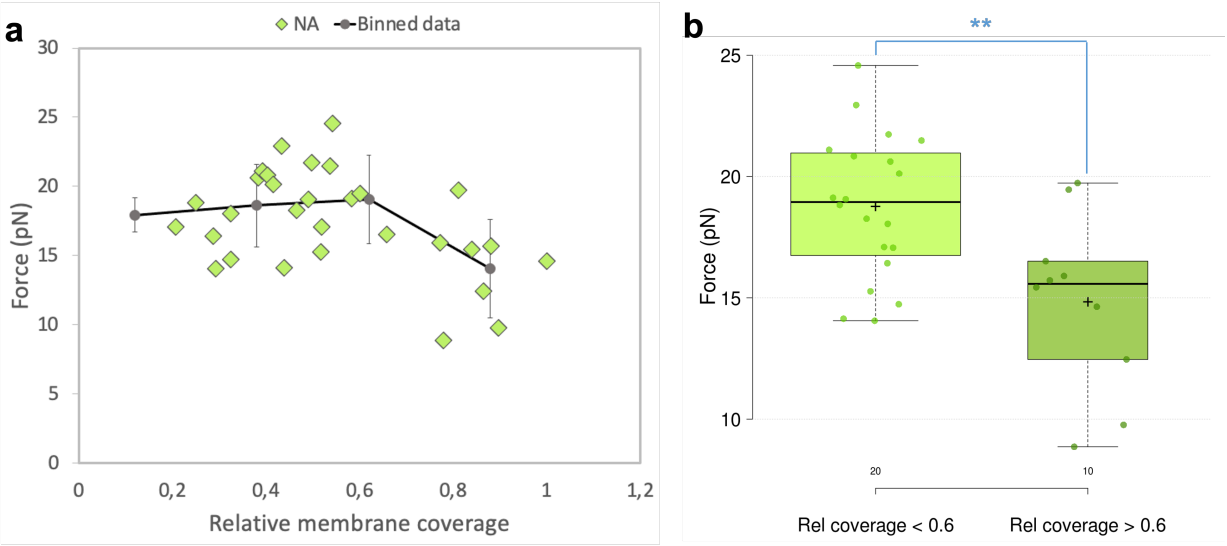

Figure 27: Equilibrium force as a function of relative membrane coverage. a) Scatter plot of force vs. relative membrane coverage for tethers pulled from NA transfected cells. The data is binned in 4 segments ([0.0-0.25), [0.25-0.50), [0.50-0.75), [0.75-1.0]). The mean value of data points in each bin is plotted at the halfway point of the bin with a gray dot, including the standard deviation in the binned section. The means are connected with a line, highlighting the trend. b) Jittered boxplot of data points grouped below and above the 0.6 mark due to the visible split in the trend at this relative membrane coverage value. The data in the two groups is normally distributed and significantly different (adjusted p-value of 0.0093), demonstrating a decrease in the tether holding force (from mean of 18.78 pN to 14.85 pN) with the increase of NA membrane coverage. Boxplot created with web-tool BoxPlotR[101]. Whiskers extend to data points that are less than 1.5 x IQR away from 1st/3rd quartile.

present in bin 1, thus this value should not be attributed great significance in this case. More data points in the low coverage range, could provide more insight into the trend in this end of the spectrum. For higher membrane coverage (>0.6), the equilibrium forces are noticeably lower. On average, the mean equilibrium force is significantly different for high vs. low-coverage cells (fig. 27b). Therefore, the data indicates that NA could indeed play a role in the budding force.

By inspecting the equilibrium forces obtained when different levels of NA is expressed in the membrane, we can uncover the effect of spontaneous curvature on the force. The real crowding effect from expression of NA on the cell membrane can however still be disguised in the data, especially as the membrane tension of the cells cannot be controlled, and could vary greatly for the pulls. Still the preliminary data obtained in these very complex cell systems indicates that some mechanism is at work which significantly lowers the equilibrium force as a function of coverage (figure 27). This suggests that further studies on the crowding affect of NA (and HA) could uncover essential information on crowding as part of the budding mechanism.

Besides the relationship between the force and the membrane coverage, the relative tube radius of pulled tethers can provide insight into the effect of crowding independently of the force measurements. As seen in figure 28a, the data clearly indicates a correlation between tube radius and membrane coverage. As the relative protein density on the membrane

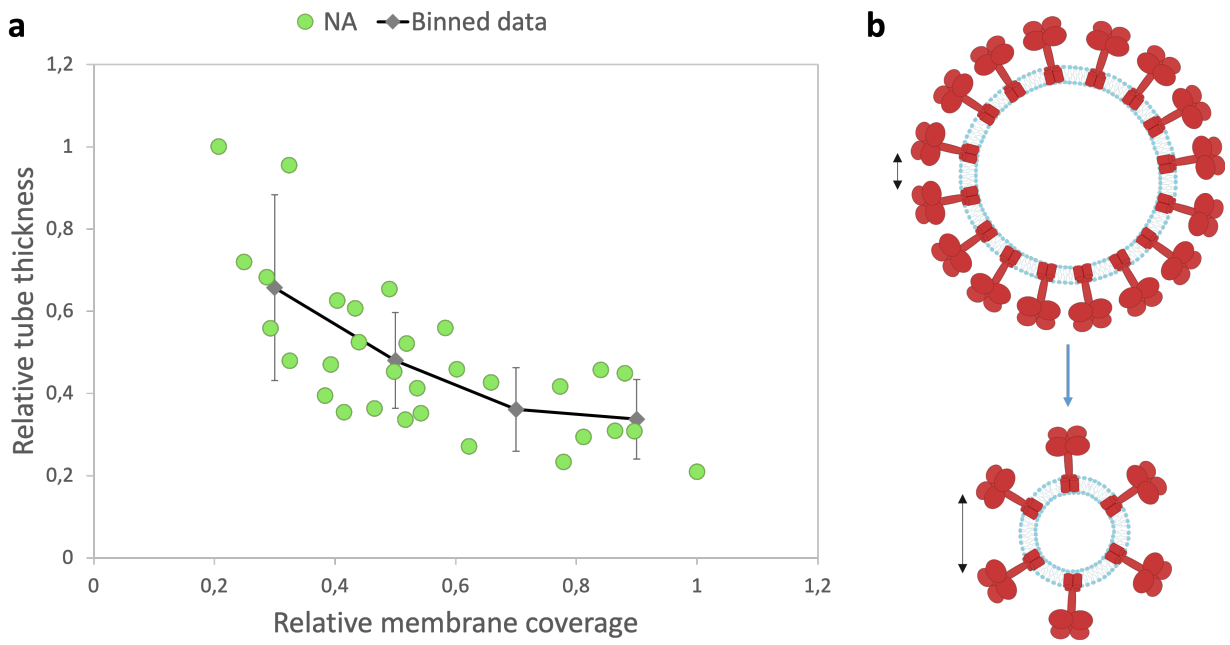

Figure 28: The effect of crowding on tether radius. a) Scatter plot of relative tube thickness vs. relative membrane coverage for tethers pulled from NA transfected cells. The data is binned in 4 segments ([0.2-0.4), [0.4-0.6), [0.6-0.8), [0.8-1.0]). Note the segment [0.0-0.2) is excluded as no data points were in this range. The mean value of data points in each bin is plotted at the halfway point of the bin with a gray dot, including the standard error in the binned section. The means are connected with a line, highlighting the trend. b) Schematic attempting to depict the notion that crowding among NA proteins could promote a decrease in membrane radius. A large radius allows for more steric interaction (top) compared to a small radius (bottom) (see arrows).

increases and thus as the crowding effect comes into play, the resulting tube radius also decreases, which in turn should result in a smaller equilibrium force. As the coverage continues to increase the corresponding decrease in radius stagnates, seemingly approaching a plateau value (figure 27a). This is expected since there is a limit to the minimization of the tether, as the membrane rigidity will counteract bending towards an infinitely narrow tether[88]. As the relative membrane protein density increases, that is with increasing contribution from the potential crowding effect, the resulting tube radius also decreases. A smaller tube radius is associated with high membrane curvature. The schematic in fig 28b sttempts to illustrate the notion that crowding, and thus steric hindrance, is potentially decreased for tubes with higher curvature. This could serve as a driver behind the crowding-induced reduction in equilibrium force. In any case, the decrease in force with radius supports the previous claim that that force decreases with protein coverage and adds evidence for crowding implications of viral protein NA.

6 Future directions

6.1 GPMV model eliminates the affect of the membrane cortex

As discussed, when working with cells, multiple variables are introduced into our membrane system, one of them being the role that actin and membrane cortex linkers play in the availability and possibly tension of the plasma membrane. The obtained results demonstrated an equilibrium force difference between control cells and the NA-expressing cells that was unexpected, as it required more force to hold the tethers with NA proteins. Some underlying interaction between the membrane cortex and NA proteins might be at play, that causes this unexpected trend, especially when considering that the increase of NA protein coverage was found to lower the force in the NA group (see figure 27 for reference). Thus, to further examine this result, the experiments should be conducted in model membranes (see figure 29a), to verify a possible correlation between steric pressure from protein collisions and the budding force, while eliminating the effect of the membrane cortex. The most appropriate choice is a system based on isolation of native plasma membranes from cells expressing the NA proteins. Such membranes are called giant plasma membrane vesicles (GPMVs) and have been used extensively to portray a naturalistic membrane composition (as compared to model GUVs) and ensure proper orientation and expression of the viral proteins in the vesicle[12]. Alternatively, the effect of the actin cortex on the membrane tension could be eliminated by disrupting the actin skeleton with latrunculin A or cytochalasin D[114,115].

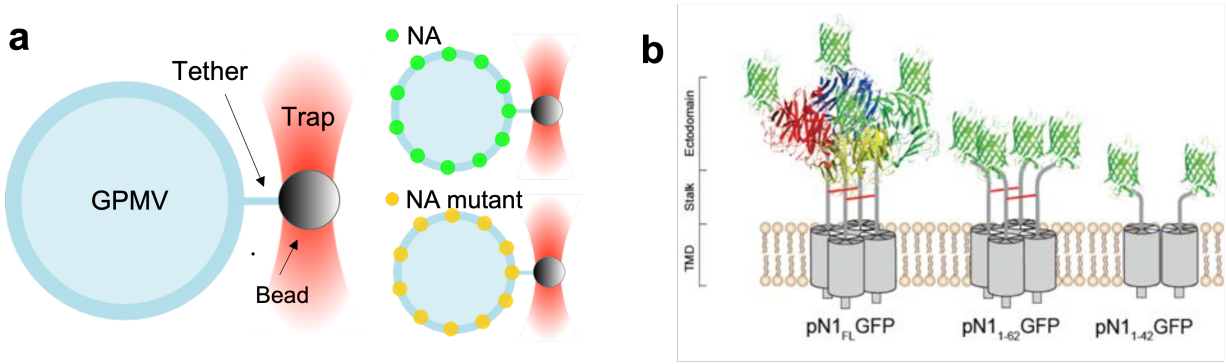

Figure 29: a) Schematic of tether pulling from GPMVs expressing NA and NA mutant. b) Mutants of NA, figure provided by Robert Daniels' group at Stockholm University.

6.2 Mutated NA can uncover bending rigidity effect

As discussed, the introduction of the TMD of NA into the membrane, could potentially affect the inherent rigidity of the membrane, making it more stiff compared to control HEK cells as observed (see figure 25 for reference). It was postulated that this contribution might mask the effect of crowding in the presented experiments. In the thesis, solely the full length NA protein was expressed and subsequently probed by force spectroscopy. However, expressing mutant NA variant could help uncover the information needed to interpret the

data properly. Firstly, with an NA-mutant consisting simply of the TMD of native NA tagged ectocellularly with GFP (see figure 29b), it is possible to isolate the effect of the TMD on the membrane rigidity. The forces of the resulting tethers can then be compared to those from NA transfected and control cells, providing data to back or challenge the postulated membrane effect. Secondly, the crowding affect could be amplified by employing a mutation of the NA protein in which the head group is preserved while the stalk is shortened significantly. This mutation results in additional lateral crowding among the expressed proteins, as the bulky group sits closer to the membrane. Both mutant proposals will aid in answering the ambiguities raised in this thesis concerning the control vs. NA tether forces (see section 5.2 for details).

6.3 Expression of multiple viral proteins

All four envelope membrane associated viral proteins are postulated to play an important role in the orchestration of viral budding[4]. Therefore, expression of multiple viral proteins together could provide more indications towards crowding, as it is highly probable that the effect will be amplified by the association or functions of the viral proteins collectedly. Therefore, the expression of various combinations of the viral proteins could be done with the presented set-up and provide interesting insight into their collected mechanism.

6.4 Improved trapping of beads

During data analysis, it was noticed that the spot in which the bead was trapped in the optical laser varied in some of the pulls (see SI, figure S35 for example). To clarify, it means that the bead was trapped in distinct places, relative to the focal area on the cells, in different pulls. Said out of focus trapping, or simply the variance in trapping, could potentially provide bias and errors in the force read-out and should be corrected for in future experiments.

In addition the tendency of the used beads to attach to large surface areas on the cell, resulting in the formation multiple tethers at once during a pull, complicated data collection. This aspect of the pulls can potentially be eliminated by switching to smaller beads. It is likely that smaller beads will make it easier to pull single tethers, as less surface contact is possible with these beads. Whether they could also improve the consistency of trapping in the same focus plane of the optical trap is unknown yet doubtful.

7 Conclusion

The budding mechanism of influenza virus A has eluded scientists for decades now, although many pieces of the puzzle have been gathered. Identifying the mechanism behind the process can advance the development of anti viral systems to combat global spread of this prevailing infection. In this thesis, the existing knowledge of NA viral protein as an important contributor to viral budding is applied in conjunction with recent studies presenting crowding as a stochastic mechanism for membrane remodelling, to elucidate the underlying factors orchestrating influenza virus budding. An assay is presented in which the effect of spontaneous curvature on membrane bending potential is analyzed with ultrasensitive force spectroscopy. The force needed to extract membrane tethers is characterized quantitatively and used to infer the effect of NA crowding on bending of the membrane. The results obtained in this thesis provide preliminary indications that NA crowding may play a role in budding, however, the effect might be obscured by many other factors following genetic induction of cellular protein expression. These include alterations in membrane mechanics or cytoskeletal effects interfering with the detachment of the plasma membrane during budding.

By employing optical tweezers, membrane tethers were successfully extracted from the surface of HEK cells and the equilibrium holding force was recorded as an indirect proxy for the tendency of the membrane to bend. A simple comparison was established between control and NA transfected cells, yielding an unexpected and significantly (adjusted p-value < 0.0001) larger force for NA containing membrane tethers. It is postulated that the crowding effect is masked by a variation in the membrane mechanics of the two probed systems, likely attributed to an increase in the membrane bending rigidity (κ) from the presence of the transmembrane domain of NA, yet alternative effects are discussed as well. These results motivates further analysis of the effect of the NA transmembrane domain on membrane properties, particularly the effect on κ.

Expression of a fluorescent GFP-tagged NA variant allowed for tracking of the relative protein coverage on the cells' membranes in addition to quantification of a relative tube radii for the formed membrane tethers. As the relative membrane coverage of NA increased, the equilibrium tether force was shown to decrease significantly (adjusted p-value $= 0.0093$) above a set threshold of 0.6 in relative membrane coverage. Simultaneously, the tube radii were reduced in line with the increasing membrane coverage of NA, seemingly approaching a plateau value, in consistency with limitations on extremely narrow tube radii as the bending rigidity opposes the curvature. The results obtained, confirming a lowering of the budding force with increasing NA coverage on the cell, are an interesting indication of NA crowding as an underlying mechanism in membrane bending, and illustrate the need for further exploration with a larger range of NA coverage on the investigated membranes.

The objective of the thesis was to determine whether membrane crowding of NA plays

a role in viral budding. The results obtained are indicative at best, establishing motivation for a more in-depth analysis of NA crowding as a putative budding mechanism. However, it is likely that expression of a combination of viral proteins will orchestrate membrane remodelling and budding in a synergistic manner and the presented assay can provide an important basis for future testing of this hypothesis.

References

1. Suttle, C. A. Viruses: unlocking the greatest biodiversity on Earth. *Genome* **56,** 542–544 (2013).
2. Smith, W., Andrewes, C. H., Laidlaw, P. P., *et al.* A virus obtained from influenza patients. *Lancet,* 66–8 (1933).
3. Paget, J. *et al.* Global mortality associated with seasonal influenza epidemics: New burden estimates and predictors from the GLaMOR Project. *Journal of global health* **9** (2019).
4. Nayak, D. P., Balogun, R. A., Yamada, H., Zhou, Z. H. & Barman, S. Influenza virus morphogenesis and budding. *Virus research* **143,** 147–161 (2009).
5. Chen, B. J., Leser, G. P., Morita, E. & Lamb, R. A. Influenza virus hemagglutinin and neuraminidase, but not the matrix protein, are required for assembly and budding of plasmid-derived virus-like particles. *Journal of virology* **81,** 7111–7123 (2007).
6. Gómez-Puertas, P., Albo, C., Pérez-Pastrana, E., Vivo, A. & Portela, A. Influenza virus matrix protein is the major driving force in virus budding. *Journal of virology* **74,** 11538–11547 (2000).
7. Rossman, J. S. & Lamb, R. A. Influenza virus assembly and budding. *Virology* **411,** 229–236 (2011).
8. Bruce, E. A. *et al.* Budding of filamentous and non-filamentous influenza A virus occurs via a VPS4 and VPS28-independent pathway. *Virology* **390,** 268–278 (2009).
9. Rossman, J. S., Jing, X., Leser, G. P. & Lamb, R. A. Influenza virus M2 protein mediates ESCRT-independent membrane scission. *Cell* **142,** 902–913 (2010).
10. Veit, M. & Thaa, B. Association of influenza virus proteins with membrane rafts. *Advances in virology* **2011** (2011).
11. Arastoo, M. R. *et al.* Phase Partitioning of influenza Virus Neuraminidase in a Model Membrane. *Biophysical Journal* **120,** 48a (2021).
12. Moreno-Pescador, G. *et al.* Curvature-and phase-induced protein sorting quantified in transfected cell-derived giant vesicles. *ACS nano* **13,** 6689–6701 (2019).
13. Pescador, G. S. M. *Membrane protein dynamics studied with optical and thermoplasmonic methods in complex and simple membranes.* PhD thesis (2019).
14. Snead, W. T. & Stachowiak, J. C. Structure versus stochasticity—the role of molecular crowding and intrinsic disorder in membrane fission. *Journal of molecular biology* **430,** 2293–2308 (2018).
15. Shurer, C. R. *et al.* Physical principles of membrane shape regulation by the glycocalyx. *Cell* **177,** 1757–1770 (2019).

16. Lai, J. C. *et al.* Formation of virus-like particles from human cell lines exclusively expressing influenza neuraminidase. *Journal of general virology* **91,** 2322–2330 (2010).

17. Liu, C., Eichelberger, M. C., Compans, R. W. & Air, G. M. Influenza type A virus neuraminidase does not play a role in viral entry, replication, assembly, or budding. *Journal of virology* **69,** 1099–1106 (1995).

18. Jauffred, L., Callisen, T. H. & Oddershede, L. B. Visco-elastic membrane tethers extracted from Escherichia coli by optical tweezers. *Biophysical journal* **93,** 4068–4075 (2007).

19. Lu, T. & Anvari, B. Characterization of the Viscoelastic Properties of Ovarian Cancer Cells Membranes by Optical Tweezers and Quantitative Phase Imaging (2020).

20. Arbore, C., Perego, L., Sergides, M. & Capitanio, M. Probing force in living cells with optical tweezers: from single-molecule mechanics to cell mechanotransduction. *Biophysical reviews* **11,** 765–782 (2019).

21. Heinrich, M. C. *et al.* Quantifying membrane curvature generation of Drosophila amphiphysin N-BAR domains. *The journal of physical chemistry letters* **1,** 3401–3406 (2010).

22. Lamb, R. A. *Influenza* in *Encyclopedia of virology* (eds Mahy, B. W. & Van Regenmortel, M. H.) (Academic Press, 2008).

23. Dou, D., Revol, R., Östbye, H., Wang, H. & Daniels, R. Influenza A virus cell entry, replication, virion assembly and movement. *Frontiers in immunology* **9,** 1581 (2018).

24. Herold, S., Becker, C., Ridge, K. M. & Budinger, G. S. Influenza virus-induced lung injury: pathogenesis and implications for treatment. *European Respiratory Journal* **45,** 1463–1478 (2015).

25. Harrington, B. & et al. Inkscape. http://www.inkscape.org/ (2004-2005).

26. Scheiffele, P., Rietveld, A., Wilk, T. & Simons, K. Influenza viruses select ordered lipid domains during budding from the plasma membrane. *Journal of Biological Chemistry* **274,** 2038–2044 (1999).

27. Barman, S. & Nayak, D. P. Lipid raft disruption by cholesterol depletion enhances influenza A virus budding from MDCK cells. *Journal of virology* **81,** 12169–12178 (2007).

28. Li, S., Eghiaian, F., Sieben, C., Herrmann, A. & Schaap, I. A. Bending and puncturing the influenza lipid envelope. *Biophysical journal* **100,** 637–645 (2011).

29. Nayak, D. P. & Barman, S. Role of lipid rafts in virus assembly and budding (2002).

30. Polozov, I. V., Bezrukov, L., Gawrisch, K. & Zimmerberg, J. Progressive ordering with decreasing temperature of the phospholipids of influenza virus. *Nature chemical biology* **4,** 248–255 (2008).

31. Samji, T. Influenza A: understanding the viral life cycle. *The Yale journal of biology and medicine* **82,** 153 (2009).

32. Lin, S., Naim, H. Y., Chapin Rodriguez, A. & Roth, M. G. Mutations in the middle of the transmembrane domain reverse the polarity of transport of the influenza virus hemagglutinin in MDCK epithelial cells. *The Journal of cell biology* **142,** 51–57 (1998).

33. McAuley, J. L., Gilbertson, B. P., Trifkovic, S., Brown, L. E. & McKimm-Breschkin, J. L. Influenza virus neuraminidase structure and functions. *Frontiers in microbiology* **10,** 39 (2019).

34. Palese, P., Tobita, K., Ueda, M. & Compans, R. W. Characterization of temperature sensitive influenza virus mutants defective in neuraminidase. *Virology* **61,** 397–410 (1974).

35. Nordholm, J., da Silva, D. V., Damjanovic, J., Dou, D. & Daniels, R. Polar residues and their positional context dictate the transmembrane domain interactions of influenza A neuraminidases. *Journal of Biological Chemistry* **288,** 10652–10660 (2013).

36. Shishkov, A. V. *et al.* The in situ structural characterization of the influenza A virus matrix M1 protein within a virion. *Protein and peptide letters* **16,** 1407–1413 (2009).

37. Sha, B. & Luo, M. Structure of a bifunctional membrane-RNA binding protein, influenza virus matrix protein M1. *Nature structural biology* **4,** 239–244 (1997).

38. Nayak, D. P., Hui, E. K.-W. & Barman, S. Assembly and budding of influenza virus. *Virus research* **106,** 147–165 (2004).

39. Iwatsuki-Horimoto, K. *et al.* The cytoplasmic tail of the influenza A virus M2 protein plays a role in viral assembly. *Journal of virology* **80,** 5233–5240 (2006).

40. Alberts, B. *et al. Molecular biology of the cell* (WW Norton & Company, 2017).

41. Kuzmin, P. I., Akimov, S. A., Chizmadzhev, Y. A., Zimmerberg, J. & Cohen, F. S. Line tension and interaction energies of membrane rafts calculated from lipid splay and tilt. *Biophysical journal* **88,** 1120–1133 (2005).

42. Sezgin, E., Levental, I., Mayor, S. & Eggeling, C. The mystery of membrane organization: composition, regulation and roles of lipid rafts. *Nature reviews Molecular cell biology* **18,** 361–374 (2017).

43. Pike, L. J. Rafts defined: a report on the Keystone Symposium on Lipid Rafts and Cell Function. *Journal of lipid research* **47,** 1597–1598 (2006).

44. Lingwood, D. & Simons, K. Lipid rafts as a membrane-organizing principle. *science* **327,** 46–50 (2010).

45. Levental, I. & Veatch, S. L. The continuing mystery of lipid rafts. *Journal of molecular biology* **428,** 4749–4764 (2016).

46. Ohkura, T., Momose, F., Ichikawa, R., Takeuchi, K. & Morikawa, Y. Influenza A virus hemagglutinin and neuraminidase mutually accelerate their apical targeting through clustering of lipid rafts. *Journal of virology* **88,** 10039–10055 (2014).

47. Nikolaus, J. *et al.* Hemagglutinin of influenza virus partitions into the nonraft domain of model membranes. *Biophysical journal* **99,** 489–498 (2010).

48. Takeda, M., Leser, G. P., Russell, C. J. & Lamb, R. A. Influenza virus hemagglutinin concentrates in lipid raft microdomains for efficient viral fusion. *Proceedings of the National Academy of Sciences* **100,** 14610–14617 (2003).

49. Sweitzer, S. M. & Hinshaw, J. E. Dynamin undergoes a GTP-dependent conformational change causing vesiculation. *Cell* **93,** 1021–1029 (1998).

50. Lee, M. C. *et al.* Sar1p N-terminal helix initiates membrane curvature and completes the fission of a COPII vesicle. *Cell* **122,** 605–617 (2005).

51. McMahon, H. T. & Gallop, J. L. Membrane curvature and mechanisms of dynamic cell membrane remodelling. *Nature* **438,** 590–596 (2005).

52. Stachowiak, J. C. *et al.* Membrane bending by protein–protein crowding. *Nature cell biology* **14,** 944–949 (2012).

53. Snead, W. T. *et al.* Membrane fission by protein crowding. *Proceedings of the National Academy of Sciences* **114,** E3258–E3267 (2017).

54. Busch, D. J. *et al.* Intrinsically disordered proteins drive membrane curvature. *Nature communications* **6,** 1–11 (2015).

55. Stachowiak, J. C., Hayden, C. C. & Sasaki, D. Y. Steric confinement of proteins on lipid membranes can drive curvature and tubulation. *Proceedings of the National Academy of Sciences* **107,** 7781–7786 (2010).

56. Carnahan, N. F. & Starling, K. E. Equation of state for nonattracting rigid spheres. *The Journal of chemical physics* **51,** 635–636 (1969).

57. Scheve, C. S., Gonzales, P. A., Momin, N. & Stachowiak, J. C. Steric pressure between membrane-bound proteins opposes lipid phase separation. *Journal of the American Chemical Society* **135,** 1185–1188 (2013).

58. Imam, Z. I. *et al.* Steric pressure among membrane-bound polymers opposes lipid phase separation. *Langmuir* **32,** 3774–3784 (2016).

59. Derganc, J. & Čopič, A. Membrane bending by protein crowding is affected by protein lateral confinement. *Biochimica et Biophysica Acta (BBA)-Biomembranes* **1858,** 1152–1159 (2016).

60. Zhao, H., Ekstr, M., Garoff, H., *et al.* The M1 and NP proteins of influenza A virus form homo-but not heterooligomeric complexes when coexpressed in BHK-21 cells. *Journal of General Virology* **79,** 2435–2446 (1998).

61. Jerome, W. G. & Price, R. L. *Basic confocal microscopy* (Springer, 2011).

62. Ruhoff, V. T. *Quantifying secondary transport at single-molecule resolution: An essay on the paper by Fitzgerald et al.* Unpublished Essay. University of Copenhagen. 2021.

63. Frackowiak, D. The jablonski diagram. *Journal of Photochemistry and Photobiology B: Biology* **2,** 399 (1988).

64. Lakowicz, J. R. *Principles of fluorescence spectroscopy* (Springer science & business media, 2013).

65. Meyvis, T. K., De Smedt, S. C., Van Oostveldt, P. & Demeester, J. Fluorescence recovery after photobleaching: a versatile tool for mobility and interaction measurements in pharmaceutical research. *Pharmaceutical research* **16,** 1153–1162 (1999).

66. Vogelsang, J. *et al.* A reducing and oxidizing system minimizes photobleaching and blinking of fluorescent dyes. *Angewandte Chemie International Edition* **47,** 5465–5469 (2008).

67. Wang, C., Gao, X. & Su, X. In vitro and in vivo imaging with quantum dots. *Analytical and bioanalytical chemistry* **397,** 1397–1415 (2010).

68. Zimmer, M. Green fluorescent protein (GFP): applications, structure, and related photophysical behavior. *Chemical reviews* **102,** 759–782 (2002).

69. Jonkman, J., Brown, C. M., Wright, G. D., Anderson, K. I. & North, A. J. Tutorial: guidance for quantitative confocal microscopy. *Nature protocols* **15,** 1585–1611 (2020).

70. Richardson, A. C., Reihani, N. & Oddershede, L. B. *Combining confocal microscopy with precise force-scope optical tweezers* in *Optical Trapping and Optical Micromanipulation III* **6326** (2006), 632628.

71. Ashkin, A. Acceleration and trapping of particles by radiation pressure. *Physical review letters* **24,** 156 (1970).

72. Jiao, J., Rebane, A. A., Ma, L. & Zhang, Y. *Single-molecule protein folding experiments using high-precision optical tweezers* in *Optical Tweezers* 357–390 (Springer, 2017).

73. Spudich, J. A., Rice, S. E., Rock, R. S., Purcell, T. J. & Warrick, H. M. Optical traps to study properties of molecular motors. *Cold Spring Harbor Protocols* **2011,** pdb–top066662 (2011).

74. Svoboda, K., Schmidt, C. F., Schnapp, B. J. & Block, S. M. Direct observation of kinesin stepping by optical trapping interferometry. *Nature* **365,** 721–727 (1993).

75. Zhang, Y. *et al.* Plasmonic tweezers: for nanoscale optical trapping and beyond. *Light: Science & Applications* **10,** 1–41 (2021).

76. Van Mameren, J., Wuite, G. J. L. & Heller, I. *Introduction to Optical Tweezers: Background, System Designs, and Commercial Solutions* in *Single Molecule Analysis: Methods and Protocols* (ed Peterman, E. J. G.) 3–23 (Springer, New York, NY, 2018).

77. Hulst, H. C. & van de Hulst, H. C. *Light scattering by small particles* (Courier Corporation, 1981).

78. Oddershede, L. *Optical Tweezers Technique* in *Handbook of Molecular Biophysics. Methods and Applications* (ed Bohr, H.) 195–214 (Wiley-VCH, Germany, 2009).

79. Gittes, F. & Schmidt, C. F. Signals and noise in micromechanical measurements. *Methods in Cell Biology* **55,** 129–156 (1998).

80. Leijnse, N., Oddershede, L. B. & Bendix, P. M. An updated look at actin dynamics in filopodia. *Cytoskeleton* **72,** 71–79 (2015).

81. Jarsch, I. K., Daste, F. & Gallop, J. L. Membrane curvature in cell biology: An integration of molecular mechanisms. *Journal of Cell Biology* **214,** 375–387 (2016).

82. Baker, M. How the Internet of cells has biologists buzzing. *Nature News* **549,** 322 (2017).

83. Prévost, C., Tsai, F.-C., Bassereau, P. & Simunovic, M. Pulling membrane nanotubes from giant unilamellar vesicles. *JoVE (Journal of Visualized Experiments),* e56086 (2017).

84. Köster, D. V. *Pulling of tethers from the cell plasma membrane using optical tweezers* in *Caveolae* 167–174 (Springer, 2020).

85. Derényi, I., Jülicher, F. & Prost, J. Formation and interaction of membrane tubes. *Physical review letters* **88,** 238101 (2002).

86. Nussenzveig, H. M. Cell membrane biophysics with optical tweezers. *European Biophysics Journal* **47,** 499–514 (2018).

87. Koster, G., Cacciuto, A., Derényi, I., Frenkel, D. & Dogterom, M. Force barriers for membrane tube formation. *Physical review letters* **94,** 068101 (2005).

88. Derényi, I. *et al. Membrane Nanotubes* in *Controlled Nanoscale Motion: Nobel Symposium 131* (eds Linke, H. & Månsson, A.) 141–159 (Springer Berlin Heidelberg, Berlin, Heidelberg, 2007).

89. Bo, L. & Waugh, R. E. Determination of bilayer membrane bending stiffness by tether formation from giant, thin-walled vesicles. *Biophysical journal* **55,** 509–517 (1989).

90. Heinrich, V. & Waugh, R. E. A piconewton force transducer and its application to measurement of the bending stiffness of phospholipid membranes. *Annals of biomedical engineering* **24,** 595–605 (1996).

91. Phillips, R., Kondev, J., Theriot, J., Garcia, H. G. & Orme, N. *Physical biology of the cell* (Garland Science, 2012).

92. Sheetz, M. P. Cell control by membrane–cytoskeleton adhesion. *Nature Reviews Molecular Cell Biology* **2,** 392–396 (2001).

93. Kozlovsky, Y. & Kozlov, M. M. Membrane fission: model for intermediate structures. *Biophysical journal* **85,** 85–96 (2003).

94. Lichtenberg, J. Y., Ling, Y. & Kim, S. Non-specific adsorption reduction methods in biosensing. *Sensors* **19,** 2488 (2019).

95. Pérez-Fuentes, L., Drummond, C., Faraudo, J. & Bastos-González, D. Adsorption of milk proteins (β-casein and β-lactoglobulin) and BSA onto hydrophobic surfaces. *Materials* **10,** 893 (2017).

96. Lumicks B. V. *Lumicks Pylake Package* 2021. `https://lumicks-pylake.readthedocs.io/en/stable/`.

97. GraphPad Software, LLC. *GraphPad Prism version 9.2.0 for Mac* 2021. `www.graphpad.com`.

98. Schindelin, J. *et al.* Fiji: an open-source platform for biological-image analysis. *Nature methods* **9,** 676–682 (2012).

99. Van Rossum, G. & Drake, F. L. *Python 3 Reference Manual* ISBN: 1441412697 (CreateSpace, Scotts Valley, CA, 2009).

100. Kluyver, T. *et al. Jupyter Notebooks - a publishing format for reproducible computational workflows* in *Positioning and Power in Academic Publishing: Players, Agents and Agendas* (eds Loizides, F. & Scmidt, B.) (IOS Press, Netherlands, 2016), 87–90.

101. Spitzer, M., Wildenhain, J., Rappsilber, J. & Tyers, M. BoxPlotR: a web tool for generation of box plots. *Nature methods* **11,** 121–122 (2014).

102. Cuvelier, D., Derényi, I., Bassereau, P. & Nassoy, P. Coalescence of membrane tethers: experiments, theory, and applications. *Biophysical journal* **88,** 2714–2726 (2005).

103. Bouvrais, H., Pott, T., Bagatolli, L. A., Ipsen, J. H. & Méléard, P. Impact of membrane-anchored fluorescent probes on the mechanical properties of lipid bilayers. *Biochimica et Biophysica Acta (BBA)-Biomembranes* **1798,** 1333–1337 (2010).

104. Dimova, R. Recent developments in the field of bending rigidity measurements on membranes. *Advances in colloid and interface science* **208,** 225–234 (2014).

105. Aimon, S. *et al.* Membrane shape modulates transmembrane protein distribution. *Developmental cell* **28,** 212–218 (2014).

106. Agrawal, H., Zelisko, M., Liu, L. & Sharma, P. Rigid proteins and softening of biological membranes—with application to HIV-induced cell membrane softening. *Scientific reports* **6,** 1–12 (2016).

107. Fowler, P. W. *et al.* Membrane stiffness is modified by integral membrane proteins. *Soft Matter* **12,** 7792–7803 (2016).

108. Raucher, D. & Sheetz, M. P. Characteristics of a membrane reservoir buffering membrane tension. *Biophysical journal* **77,** 1992–2002 (1999).

109. Khatibzadeh, N., Spector, A. A., Brownell, W. E. & Anvari, B. Effects of plasma membrane cholesterol level and cytoskeleton F-actin on cell protrusion mechanics. *PloS one* **8,** e57147 (2013).

110. Paraschiv, A. *et al.* Influence of membrane-cortex linkers on the extrusion of membrane tubes. *Biophysical Journal* **120,** 598–606 (2021).

111. Leijnse, N., Oddershede, L. B. & Bendix, P. M. Helical buckling of actin inside filopodia generates traction. *Proceedings of the National Academy of Sciences* **112,** 136–141 (2015).

112. Senikoglou, P. *Investigation of membrane tension as a signaling cue for immune cells.* MA thesis (University of Copenhagen, 2020).

113. Pontes, B. *et al.* Cell cytoskeleton and tether extraction. *Biophysical journal* **101,** 43–52 (2011).

114. Coué, M., Brenner, S. L., Spector, I. & Korn, E. D. Inhibition of actin polymerization by latrunculin A. *FEBS letters* **213,** 316–318 (1987).

115. Cooper, J. A. Effects of cytochalasin and phalloidin on actin. *Journal of Cell Biology* **105,** 1473–1478 (1987).

8 Supplementary information

8.1 Fluorescence spectra

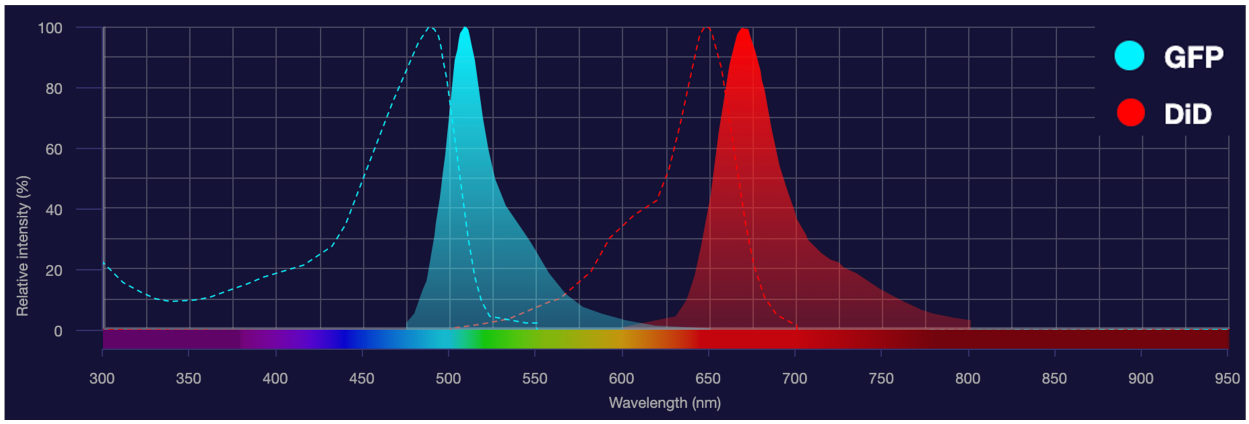

Figure S30: Combined absorption and emission spectra of GFP and DiD. Created in ThermoFisher Scientific Fluorescence SpectraViewer.

8.2 Confocal microscopy setting specifications

- NA setting: AOTF 633 = 10%, reflection mode, PMT (628-642), gain = 1000V, AOTF 488 = 20%, PMT (497-578), gain = 500V, Scan-BF PMT trans gain = 250V.
- DiD setting: AOTF 633 = 15%, PMT (641-765), gain = 500V, AOTF 514 = 15%, reflection mode, PMT (508-521), gain = 1000V, Scan-BF PMT Trans gain = 250V.
- Control: AOTF 633 = 20%, reflection mode, PMT (628-642), gain = 500V, AOTF 496 = 35%, AOTF 514 = 35%, Scan-BF PMT Trans gain = 252V.

8.3 Comparison of multiple force traces

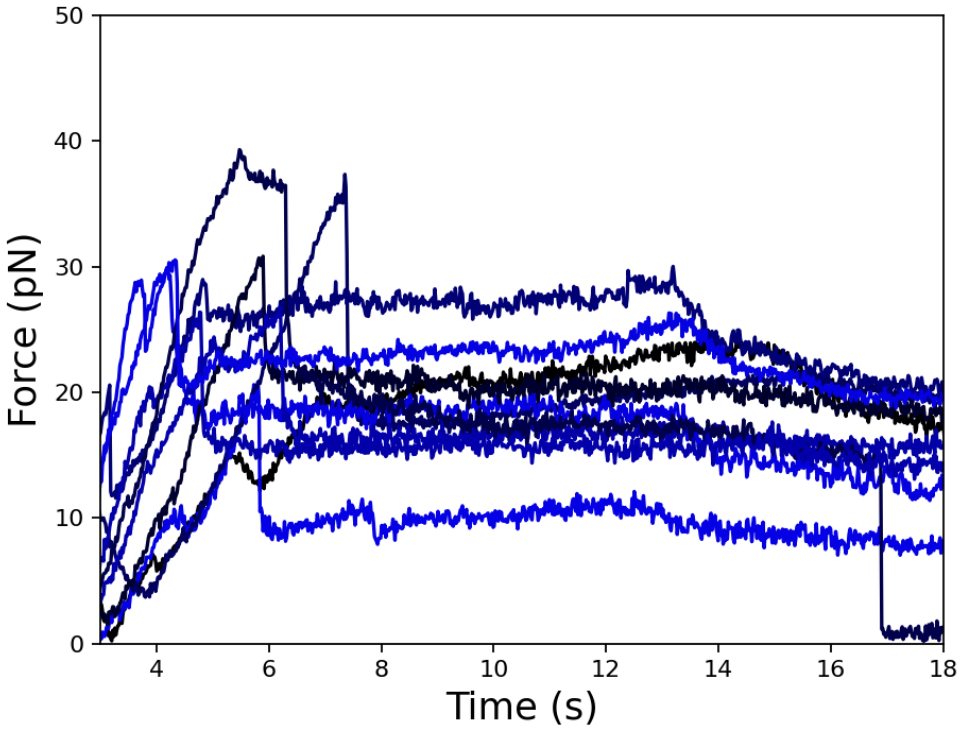

Figure S31: 10 example force profiles plotted for NA-transfected cells, demonstrating the various shapes obtained in experiments.

8.4 Tether equilibrium force extraction prior to tether snapping

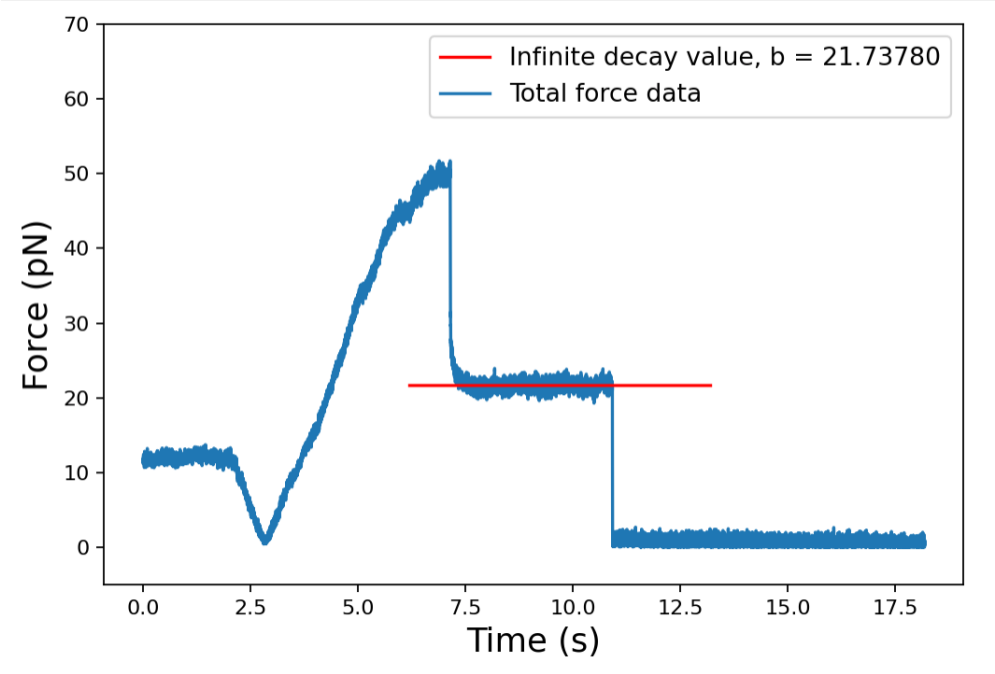

Figure S32: Force profile showing a clear tether snapping around 11 s. The prior data points (7.5 to 11 s.) after the force drop is used to quantify the equilibrium force in this case.

8.5 Data normality test specifications

Normality and Lognormality Tests Tabular results		A	B	C
		Empty	NA FL	DiD
		Y	Y	Y
9	**Anderson-Darling test**			
10	A2*	0.3681	0.2095	0.5758
11	P value	0.3998	0.8479	0.0899
12	Passed normality test (alpha=0.05)?	Yes	Yes	Yes
13	P value summary	ns	ns	ns
14				
15	**D'Agostino & Pearson test**			
16	K2	5.018	1.153	1.685
17	P value	0.0813	0.5618	0.4306
18	Passed normality test (alpha=0.05)?	Yes	Yes	Yes
19	P value summary	ns	ns	ns
20				
21	**Shapiro-Wilk test**			
22	W	0.9403	0.9799	0.8429
23	P value	0.1822	0.8231	0.0807
24	Passed normality test (alpha=0.05)?	Yes	Yes	Yes
25	P value summary	ns	ns	ns
26				
27	**Kolmogorov-Smirnov test**			
28	KS distance	0.09627	0.07873	0.2607
29	P value	>0.1000	>0.1000	>0.1000
30	Passed normality test (alpha=0.05)?	Yes	Yes	Yes
31	P value summary	ns	ns	ns

Figure S33: Test specifications from the normality test performed on the data (alpha = 0.05). Note that all tests are passed, confirming that the data is normally distributed.

8.6 One-way ANOVA results with all data points

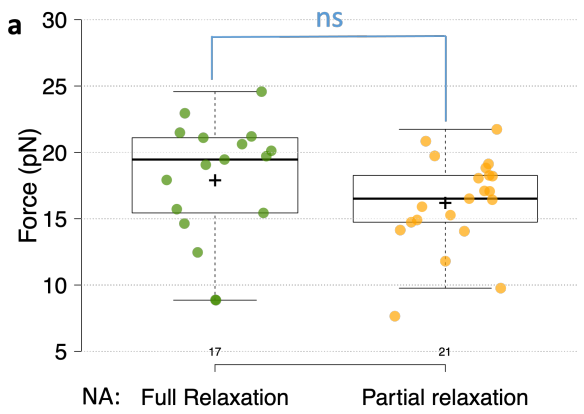

Unpaired t test with Welch's correction	
P value	0.2175
P value summary	ns

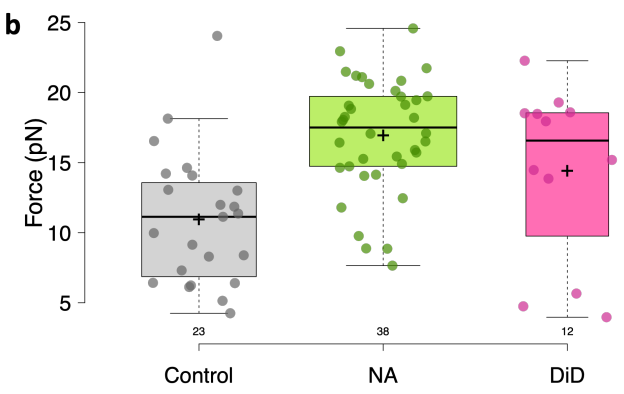

Dunnett's T3 multiple comparisons test	Summary	Adjusted P Value
Empty vs. NA FL	**	0.0031
Empty vs. DiD	ns	0.5687
NA FL vs. DiD	ns	0.4841

Figure S34: Statistical analysis prior to the removal of uncertain data points based on tube intensity. a) Jittered boxplot of full vs. partial relaxation data points and corresponding non significant p-value of 0.2175. b) Jittered boxplot of the force distribution in each group. Obtained adjusted p-values are listed in the table. Note, that the adjusted p-value shows that the difference in the empty (control group) vs. NA FL (NA group) mean is still significant (adjusted p-value = 0.0031).

8.7 Variations in the focus of trapped beads

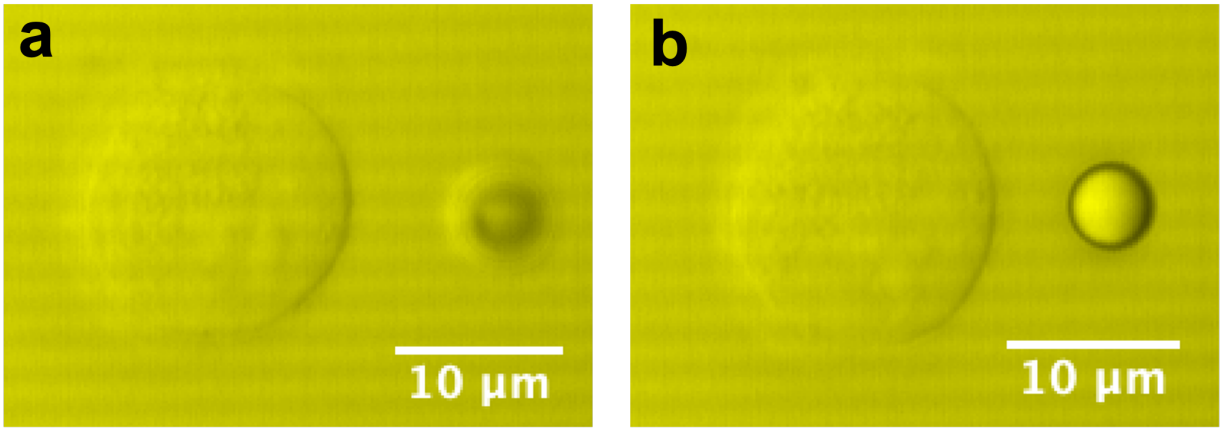

Figure S35: a) & b) Images showing trapping of a bead in different focus spots in the trap.